School of Chemistry & Physics

Pietermaritzburg campus

IMPROVED COLLECTION OF PHOTOGENERATED CURRENT USING BI-METAL NANOPARTICLES

MSc Dissertation

by

Candidate: Ncedo Jili

January 2024

IMPROVED COLLECTION OF PHOTOGENERATED CURRENT USING BI-METAL NANOPARTICLES

by

NCEDO JILI

2024

A dissertation submitted to the School of Chemistry and Physics, College of Agriculture, Engineering and Science, University of KwaZulu-Natal, PMB, for the degree of Master of Science(MSc)

As the candidate's supervisor, I have approved this dissertation for submission

... **Date................................**

Supervisor:
Prof. Genene Tessema Mola

Abstract

The energy demand has been continuously growing owing to the shortage of sources of traditional energy (such as fossil fuels), due to the growing population of the world, and increased industrialization, which prompted the need for more energy. However renewable energy (such as photovoltaics) has attained attention due to its reliance on the infinite energy source (sun) which provides an hour long energy flow that fulfil the yearly energy of the glob. Not only that, renewable energy sources offer clean energy, that is meant to contribute to decarbonization in the future and reduce environmental changes. Solar cell materials that can effectively capture photons and conduct charges are continuously investigated for the last six decades. Contrarily to silicon based solar cells, organic solar cells are among the most promising solar cells in terms of offering cheap device fabrication, flexibility, high absorption, etc. However, these solar cells still suffer from low efficiency compared to traditional silicon solar cells due to poor absorption, low mobility, and poor stability. Numerous strategies have been employed to improve the efficiency of OSC devices, these include Ternary OScs, Tandem OSCs, and the inclusion of nanoparticles in OSC devices. Nanoparticles remain the best candidate to feature in OSC devices because Tandem OSCs require multi-absorber layers which leads to high device cost, whereas nanoparticles can be produced at a small scale and still offer good results. This study takes advantage of the features offered by the nanoparticles and uses them to investigate the effect of Nickel doped with cobalt bi-metal nanoparticles(Ni/Co BMNPs) in the PEDOT:PSS buffer layers of the P3HT: PCBM-based devices. Solar cells were successfully fabricated with four different concentrations of Ni/Co BMNPs as 0.05 %(0.5 mg), 0.15 %(1.5 mg), and 0.25 %(2.5 mg). Significant improvements were achieved for the 0.05% with the Fill factor of 58.52 %, and current density of 15.31 mA/cm^2, and maximum efficiency of 5.05 % which displayed 67.8 % improvement from the undoped device. The investigation was further conducted by simulation program called SCAPS to confirm yhe contribution of the metal nanoparticles on the device performance. The results were reproduced in SCAPS where the energy band gap of the P3HT:PCBM and the shallow conduction density of electrons of the PEDO:PSS were simultaneously varied. All results are comparable with the experimental results and found to be similar. The device that was made to mimic the 0.05 % device produced a FF of 57.76 %, J_{sc} of 15.76 mA/cm^2, and maximum efficiency of 5.76 % which displayed 88 % improvement from the undoped device. This study further provides factors that contributed to the high/low device performance due to the inclusion of the BMNPs in the OSC device and some of the necessary background and theory are provided to support these findings.

Abbreviations

ABL	Absorber Layer
Al	Aluminium
BMNPs	Bi-Metal Nanoparticles
CO_2	Carbon dioxide
$Co(N0_3)_2$	Cobalt Nitrate
EB	Binding Energy
EQE	External Quantum Efficiency
ETL	Electron Transport Layer
FF	Fill Factor
HOMO	Highest Occupied Molecular Orbital
IPCE	Incident Photon to electron Conversion Efficiency
ITO	Indium Tin Oxide
LiF	Lithium Fluoride
LSPR	Localized Surface Plasmon Resonance
LUMO	Lowest Unoccupied Molecular Orbital
MNPs	Metal Nanoparticles
$NaBH_4$	Sodium Borohydride
$Ni(N0_3)_2$	Nickel Nitrate
Ni/Co BMNPs	Nickel doped with cobalt Bi-Metal Nanoparticles
NPs	Nanoparticles

NREL	National Renewable Energy Laboratory
OSCs	Organic Solar Cells
P3HT:PCBM	poly(3-Hexylthiophene).:[6,6]-Phenyl-C61-Butyric Acid Methyl Ester
PCE	Power Conversion Efficiency
PEDOT:PSS	Poly(3,4-Ethylenedioxythiophene) Polystyrene Sulfonate
PIRET	Plasmon Induced Resonance Energy Transfer
SCAPS	Solar cell Capacitance Simulator
SEM	Scanning Electron Microscopy
SPCLC	Space Charge Limited Current
TEM	Transmision Electron Microscopy

Declaration

I, **NCEDO JILI**, declare that

1. The research reported in this desertation, except where otherwise indicated, is my original research
2. This dissertation has not been submitted for any degree or examination at any other university
3. This thesis does not contain other persons' data, pictures, graphs or other information, unless specifically acknowledged as being sourced from other persons.
4. This dissertation does not contain other persons' writting, unless spscifically acknowledged as being sources from other researchers. Where other written sources have been quoted, then:
    (a) Their words have been rewritten but the general information attributed to them has been referenced
    (b) Where their exact words have been used, then their writting has been placed in italics and inside quotation marks, and referenced.
5. This dissertation does not contain, text, graphics or tables copied and pasted from the internet,unless specifically acknoledged, and the source being detailed in the dissertation and in the referencies sections

[redacted]............................

Signiture

Acknowledgement

I'd want to express my gratitude to my supervisor, Prof. Genene Tessema Mola, for his unwavering support and advice during my research journey. He has made significant scholarly contributions to me, and he has pushed me to write publications, and I would like to thank him and Dr. Nkosinathi Dlamini for their guidance in the completion and publishing of my first article. I would not have achieved what I have if it hadn't been for his mentoring. I'm quite thankful to the University of Kwazulu Natal, PMB campus, for enabling me to use their facilities and resources while completing my master's degree.I would especially like to express my gratitude to the following people: my material science laboratory groups that introduced me to the lab; the physics department, especially the staff members who were always willing to help; my postgraduate colleagues with whom I shared the P3B office and the wonderful experience we had, especially in the year 2022. My heartfelt gratitude goes to my mother and father, my two brothers, cousins, and sisters, my Aunts, and my grandmothers from both my mother's and father's sides. My family has been there for me from the beginning of my schooling to the present. I extend my gratitude to all those who directly or indirectly contributed to the completion of this thesis. Finally, I express my gratitude to the all-powerful God for giving me life, happiness, endurance, understanding, and strength.

Contents

List of Figures

List of Tables

Chapter 1

1 Introduction

1.1 Renewable energy

The Industrial Revolution led to emerge more advanced technologies, which made life easy and brought more wealth that grew the economy. However, there is high energy demand to power such technologies, and the current energy sources (fossil fuels) are finite and emit greenhouse gases such as CO_2. The emission of greenhouse gases can lead to severe environmental changes like global warming whose consequences are evident by the rise of sea levels due to the melting of onshore ice shields, water shortage, desertification, and the collapse of the ecosystem, etc [3]. Due to all these severe impacts of burning fossil fuels on the environment, an alternative source of energy that contributes to decarbonization, such as renewable energy is currently receiving immense attention. The replacement of fossil fuels with renewable energy sources is expected to reduce CO_2 emission by 75 % by 2050 [2, 3, 5, 10] which brings us to the levels in 1985. Renewable energy sources not only protect the environment but also contribute to the fast-growing world economy and bring stability to nature. The renewable energy technologies can be produced at small scales and, in a short time. Some renewable technologies include windmills, photovoltaics, and nuclear power [4, 6, 7, 9, 13], etc. Among these renewable technologies, photovoltaic technology is regarded as the most promising technology owing to the abundant energy coming from the sun. The earth receives $10^{20}J$ of magnitude of energy from the sun per hour which is equivalent to the amount of energy used in the world per year. This energy can be converted to electricity by solar cell devices. The excess energy spreads around the globe and can be absorbed by plants, or by the earth's surface, or can be reflected into space [4]. Solar cells made their breakthrough after the introduction of the p-n junction by William B. Shockley, Walther H. Brattain, and John Bardeen (Nobel Prize for the transistor in 1956)[1]. With the advent of new technologies and the attention they are currently receiving, their performance has improved since their launch by Bell Labs in

1954 [8, 10, 25, 27]. The performance of different types of solar cells reported on the

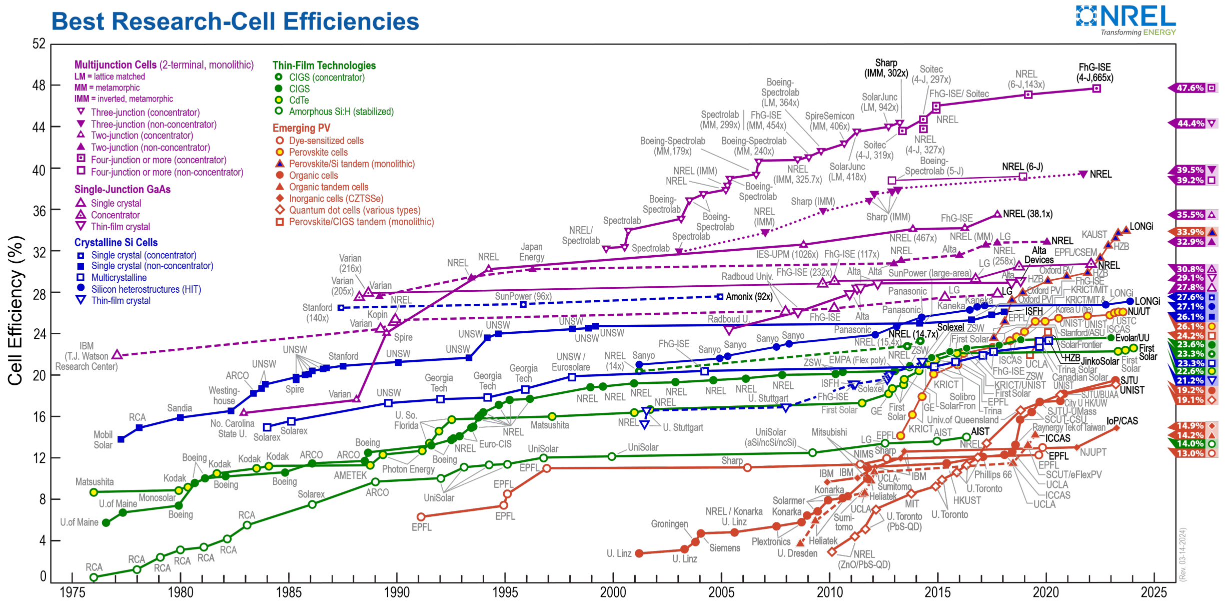

Figure 1: Best research cell efficiencies recorded by NREL from 1974 to 2023, Figure and caption taken from NREL website in ref [11].

NREL website is shown in Figure 1, with the Multijunction solar cells being the most efficient solar cells, with minimum efficiency records of 35.5 % and maximum efficiencies of 47.6 %. In terms of efficiency, Single-Junction GaAs solar cells rank second. The minimum efficiency of 27.8 % and maximum efficiency of 30.8 % are reported for these solar cells. Crystalline Si Cells is the third most popular solar cell. The lowest efficiency of 21.2 % and the highest efficiency of 27.6 % were reported for these solar cells. Thin-Film Technologies, with a record minimum efficiency of 14.0 % and a maximum efficiency of 23.6 %, is the second-last efficient solar cell. Finally, for Emerging photovoltaics (PV) cells, their reported minimum and maximum efficiency are 13 % and 33.9 %, respectively. According to Figure 1, which provides a detailed overview of each of these solar cells' progress, some of these solar cells were launched as early as 1976, some in the 1990s, some in the early and late 2000s, and some had their progress end before 2023 owing to a lack of research. In terms of efficiency and research, organic solar cells are currently among the fastest-growing solar cells.

1.1.1 Progress in organic solar cells

Organic solar cells are one of the new emerging solar cell technologies that have attracted the attention of scientists and engineers as well as industries. These new and emerging technologies including perovskite, dye-synthesized solar cells, and organic solar cells (OSC) brought advantages in terms of cost, and stability. OSC is the leading technology in terms of offering low cost, portability,flexibility [14, 16, 17, 18, 19] etc. These solar cells came into existence after the discovery of conducting polymers in the 1970s by Heeger et al. who were later awarded with Nobel prize in 2000s [10, 12]. OSCs are often fabricated in one of the three main device structures (see Figure 2). The first OSC was made in the 1980s from a single active layer sandwiched between the two electrodes (see Figure 2a), which has produced a PCE as low as 0.1 %[50] due to the challenges in separating excitons. Tang introduced a bilayer heterojunction structure (Figure 2b) in 1986 [15, 38, 46, 50], which was regarded as a significant advancement in the area of OSCs at the time. This structure used copper phthalocyanine as the donor (D) and perylene tetracarboxylic derivate as the acceptor (A). Using copper phthalocyanine and perylene tetracarboxylic derivate as active layers, this bilayer heterojunction device produced a PCE of less than 1 %. Compared to inorganic solar cell PCE, this efficiency was regarded as small. Short exciton diffusion lengths (ranging from 1-10 nm) and exciton lifetime were responsible for low PCE in OSC [41, 46]. Moreover, the use of a thin organic photoactive layer

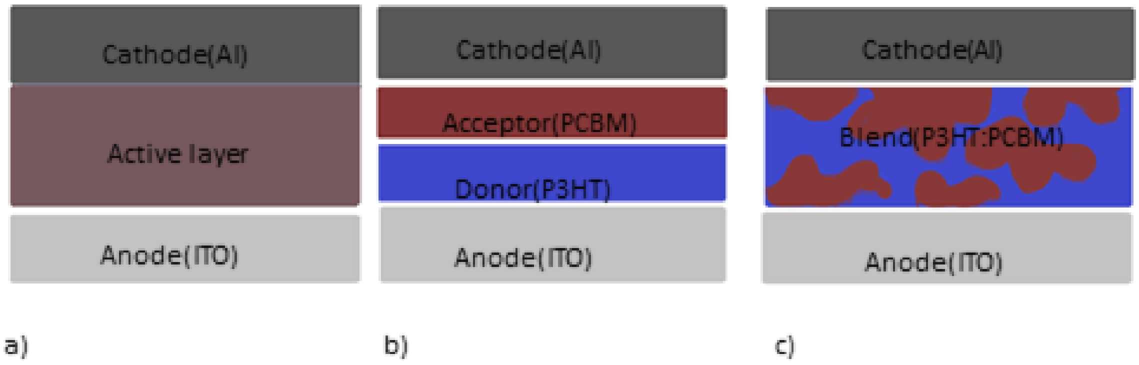

Figure 2: Different structures of organic solar cells, a) Single layer structure,b) bi-layer, c) Bulk-heterojunction structure(blend).

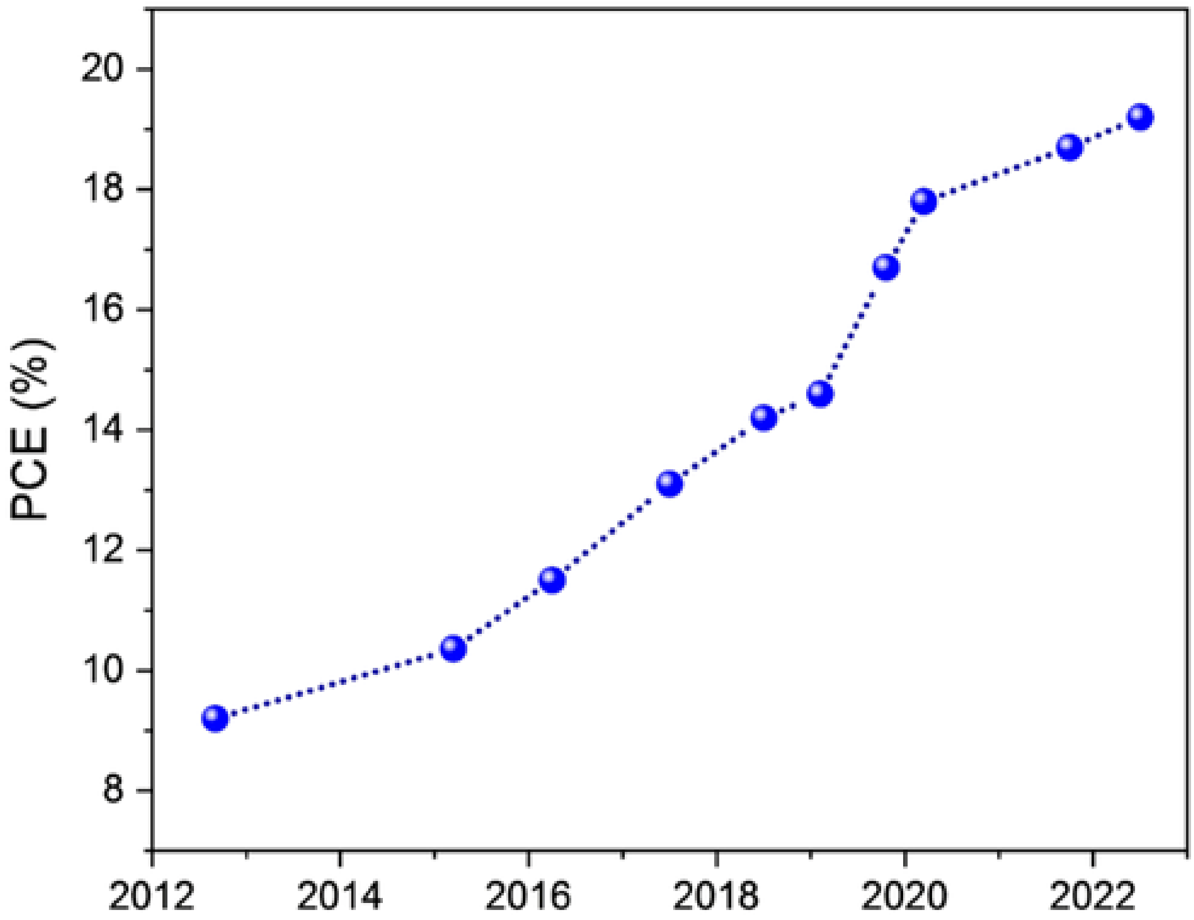

Figure 3: Growth in efficiency of organic solar cells from 2012 to 2022.

owing to poor absorption. The new device architecture known as bulk-heterojunction was introduced in 1995 [15] by Yu et al It involves blending the donor and acceptor material(see Figure 2c) bringing the interfaces close enough to allow the exciton separation before recombination. The use of bulk heterojunction design of Organic Solar Cells led to improved efficiency as close as 6 %.However, with the introduction of small molecules and non-fullerene acceptors, the power conversion efficiency grew from less than 1 %in 1990 to ($\sim$ 20%) [15, 16, 17, 19] in 2022 as shown in Figure 3 taken from ref [14]. Even with the advent of BHJ, the problems of poor absorption and conductivity remain, thus research is currently concentrating on the insertion of nanoparticles in organic devices to increase absorption and conductivity.

Chapter 2

2 Semiconductor characteristics and devices

A semiconductor is a material that has an electrical conductivity between that of a metal and an insulator [20]. One of the parameters that characterizes the semiconductor is the energy band gap which can be referred to as the forbidden space between the conduction band and valence band. The occupation of electrons in the conduction band depends on the temperature, At zero kelvin the conduction band is empty while the valence band is fully occupied [1]. At temperature T, the density of electrons in the conduction band is varied according to [1, 9, 21, 22, 23, 24]

$$n = 2\left(\frac{m_e k_B T}{2\pi\hbar^2}\right)^{\frac{3}{2}} \exp\left(\frac{-(E_c - E_F)}{k_B T}\right) = N_C \exp\left(\frac{-(E_c - E_F)}{k_B T}\right) \tag{1}$$

Similarly,the concentration of holes in the valence band is defined as

$$p = 2\left(\frac{m_h k_B T}{2\pi\hbar^2}\right)^{\frac{3}{2}} \exp\left(\frac{(E_V - E_F)}{k_B T}\right) = N_V \exp\left(\frac{(E_V - E_F)}{k_B T}\right) \tag{2}$$

Where m$_e$ is the effective mass of electrons,m$_h$ is the effective mass of holes, K$_B$ is the Boltzmann constant, T is the temperature, $\hbar$ is the reduced Planck's constant, E$_C$ conduction band energy, E$_V$ is the valence band energy, E$_F$ is the fermi-level energy, N$_C$ is the conduction effective density of states, and N$_V$ is valence effective density of states. In an intrinsic semiconductor, the concentration of electrons in the conduction band is equal to the concentration of holes in the valence band $n = p = n_i$[1, 9, 21, 22, 23]. By multiplying eq.1 and eq.2 it can be shown that the intrinsic carrier concentration depends exponentially on Eg/2k$_B$T, where Eg is the energy band gap defined as Eg = E$_C$−E$_V$.

$$np = {n_i}^2 = 4\left(\frac{K_B T}{2\pi\hbar^2}\right)^3 (m_h m_e)^{\frac{3}{2}} \exp\left(\frac{(-E_C + E_V)}{K_B T}\right) \tag{3}$$

By putting a square root on eq.3 we get

$$n_i = 2\left(\frac{k_B T}{2\pi\hbar^2}\right)^{\frac{3}{2}} (m_h m_e)^{\frac{3}{4}} \exp\left(\frac{-E_g}{k_B T}\right) \tag{4}$$

The Fermi energy can be obtained by equating eq.1 to eq.2

$$N_C \exp\left(\frac{-(E_c - E_F)}{k_B T}\right) = N_V \exp\left(\frac{(E_V - E_F)}{k_B T}\right) \tag{5}$$

Putting the natural log in both sides of eq.5, and rearranging, we can arrive at the following fermi energy equation

$$E_F = \frac{(E_V + E_C)}{2} + \frac{k_B T}{2} ln\left(\frac{N_C}{N_V}\right) \tag{6}$$

If $N_C = N_V$ then $E_F = \frac{(E_V+E_C)}{2}$, and E_F lies close to the middle of the forbidden gap as shown in Figure 4a. The intrinsic semiconductors remain non-conducting until small dopants are introduced. Doped semiconductors with acceptor atoms or donor atoms to

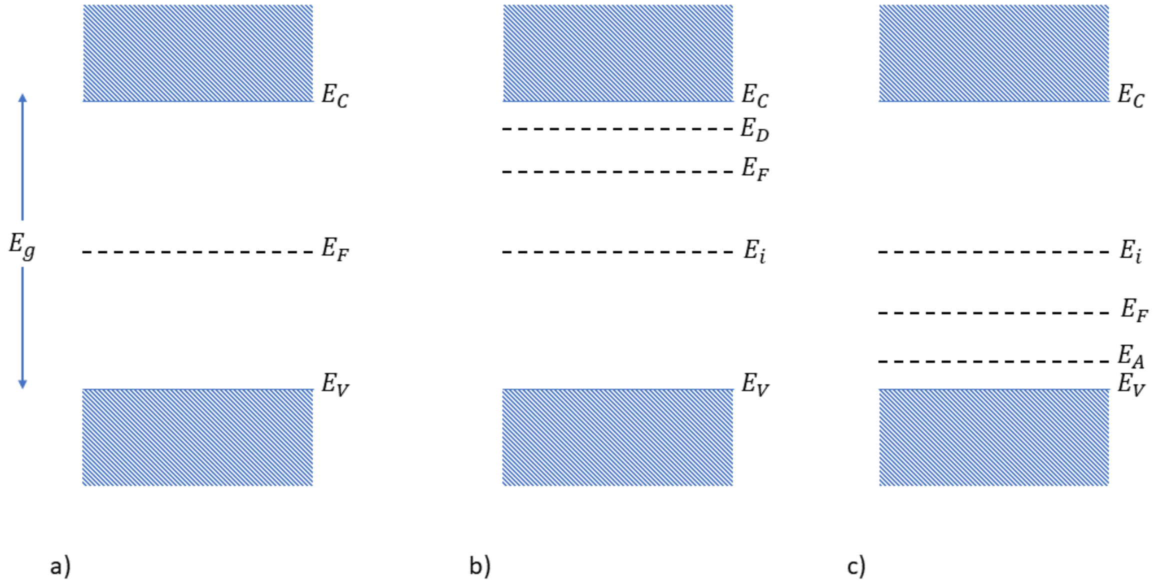

Figure 4: The energy diagram showing the intrinsic and extrinsic semiconductors, a) An intrinsic semiconductor with the fermi-level centered in the forbidden region,b) Semiconductor doped with donor atoms resulting in the fermi-level shifting up close to the conduction band,c) Semiconductor doped with acceptor atoms resulting in the fermi-level shifting down close to the valence band.

set up their conductive property are known as extrinsic semiconductors. For instance, an array of Silicon atoms with no impurities cannot conduct carriers due to the balance of charges in the atoms. Silicon has four valence electrons, in a crystal array, all these electrons are paired with the neighboring Silicon atoms which results in the stability of these atoms. These electrons are immobile or are constrained between the atoms since they are used to form the bonds between the atoms. The conductive properties of Silicon change when small impurities such as phosphorous or arsenic are introduced into the Silicon crystal structure to replace the Silicon atom. Phosphorous has five valence electrons, when it replaces the Silicon atom, only four of the five valence electrons fit in the crystal structure the fifth is free to move throughout the crystal [22, 25, 26]. A semiconductor doped with small amounts of phosphorous can be imagined as containing positively charged atoms and electrons that are free to wander throughout the semiconductor, which therefore alters the conductive properties of the material. This type of semiconductor is called an n-type semiconductor because the doped impurities contribute mobile negative charge (electrons)(see Figure 5a). In the p-type semiconductor, the doped impurities contribute positive charge(holes)(see Figure 5a), for instance, a Boron atom has three valence electrons when it is doped into the silicon crystal structure, and an electron from Silicon occupies a hole in Boron (boron becomes negative since it has gained an electron) leaving a hole behind [22, 25, 26], An electron from a neighboring silicon atom can move into this hole, and the hole moves to another Silicon atom, In this way, a positively charged hole can wander through the crystal. Therefore, this type of semiconductor can be viewed as containing immobile, negatively charged boron atoms and an equal number of positively charged, mobile holes. Because of the mobile holes, the semiconductor can conduct electricity. The introduction of defects such as donor atoms in the Silicon crystal structure can lead to the **complete ionization** of donor impurities in such semiconductors at room temperature suggesting an equal number of electrons in the conduction as the number of impurity atoms[22]. If we let N_D the donor concentration of atoms, and equate it to eq.1

we obtain

$$n = N_C \exp\left(\frac{-(E_c - E_F)}{k_B T}\right) = N_D \tag{7}$$

It can be noted in Figure 4b that the Fermi level shifts upwards due to the introduction of the donor level [25, 42]. It is necessary to express the concentration of electrons and holes as the intrinsic carrier concentration n$_i$ and intrinsic Fermi level(E$_i$) as they are used as a reference point for the discussion of the extrinsic carriers. Therefore multiplying eq.7 by $\exp\left(\frac{-E_i}{k_B T}\right)\exp\left(\frac{E_i}{k_B T}\right)$ yields

$$n = N_C \exp\left(\frac{-(E_c - E_F)}{k_B T}\right) \exp\left(\frac{-E_i}{K_B T}\right) \exp\left(\frac{E_i}{k_B T}\right) \tag{8}$$

$$n = N_C \exp\left(\frac{(E_i - E_C)}{k_B T}\right) . \exp\left(\frac{E_F - E_i}{k_B T}\right) \tag{9}$$

$$n = n_i . \exp\left(\frac{E_F - E_i}{k_B T}\right) \tag{10}$$

Similarly, for the p-type impurity concentration (holes), one can arrive at the following equation after derivation.

$$p = p_i . \exp\left(\frac{E_F - E_i}{k_B T}\right) \tag{11}$$

When these semiconductors are brought into contact, a p-n junction is formed. The free electrons from the n-material and free holes from the p-type material close to the junction diffuse across the junction (see Figure 5b) and combine, leading to a **diffusion current**, which occurs due to a large carrier concentration gradient at the junction. This carrier diffusion is caused by thermal energy since there is no external field. On the other hand, the potential gradient is created across the p-n junction which results in the creation of a **drift current** which counteracts the diffusion current.

2.1 Charge transport in Semionductors

2.1.1 Diffusion current

The currents due to diffusion of electrons from an n-type material to a p-type and holes from a p-type material to an n-type are given by [23, 25, 27, 28, 31]

$$J_{diff,n} = eD_n \frac{\partial n}{\partial x} \tag{12}$$

$$J_{diff,p} = -eD_p \frac{\partial p}{\partial x} \tag{13}$$

D_n, D_p are the diffusion coefficients given by the Einstein relations

$$D_n = \frac{k_B T}{e} \mu_n \tag{14}$$

$$D_p = \frac{k_B T}{e} \mu_p \tag{15}$$

μ_n and μ_p are electron and hole mobilities respectively.
The drift current densities are given by

$$J_{drift,n} = e\mu_n nE \tag{16}$$

$$J_{drift,p} = e\mu_p pE \tag{17}$$

Where E is the electric field. The total current due to electrons is given by the sum of the drift and diffusion currents.

$$J_n = J_{diff,n} + J_{drift,n} = e\mu_n nE + eD_n \frac{\partial n}{\partial x} \tag{18}$$

The total current due to holes is the sum of eq.13 and eq.17

$$J_p = J_{diff,p} + J_{drift,p} = e\mu_p pE - eD_p \frac{\partial p}{\partial x} \tag{19}$$

The combined total current is given by the sum of eq. 18 and eq.19

$$J = J_n + J_p = (\mu_n n + \mu_p p)\, eE + \left(D_n \frac{\partial n}{\partial x} - D_p \frac{\partial p}{\partial x} \right) e \tag{20}$$

When there is a balance(at equilibrium) of charges in the positive and negative charge layers on the two sides of the junction, An electric field set up by these layers prevents any further movement of charge across the junction [27], and all charge flow quickly stops(such that the current is zero), creating a region with no charge called the **depletion region(space charge region)**(Figure 5b).

2.2 The p-n junction under external bias voltage

2.2.1 Reverse bias p-n junction

When an external load like a battery is connected across these semiconductors, such that the battery's positive terminal is connected to the n-type material, and the negative terminal is connected to the p-type semiconductor. The positive charges in the battery's positive terminal will attract the negative charges in the n-type material, forcing them to migrate away from the depletion region. Likewise, the negative charges from the negative terminal of the battery will attract the positive charges from the p-type material forcing them to migrate away from the depletion region as a result the depletion region and the potential barrier will expand, allowing the minority of charges to pass across this region(See Figure 6b).

2.2.2 Forward bias p-n junction

The battery is connected across these semiconductors such that the positive terminal of the battery is connected to the p-type material and the negative terminal is connected to the n-type semiconductor. The positive charges in the positive terminal of the battery will repel the positive charges in the p-type material forcing them to migrate toward the depletion region. Likewise, the negative charges from the negative terminal of the battery will repel the negative charges from the n-type material forcing them to migrate

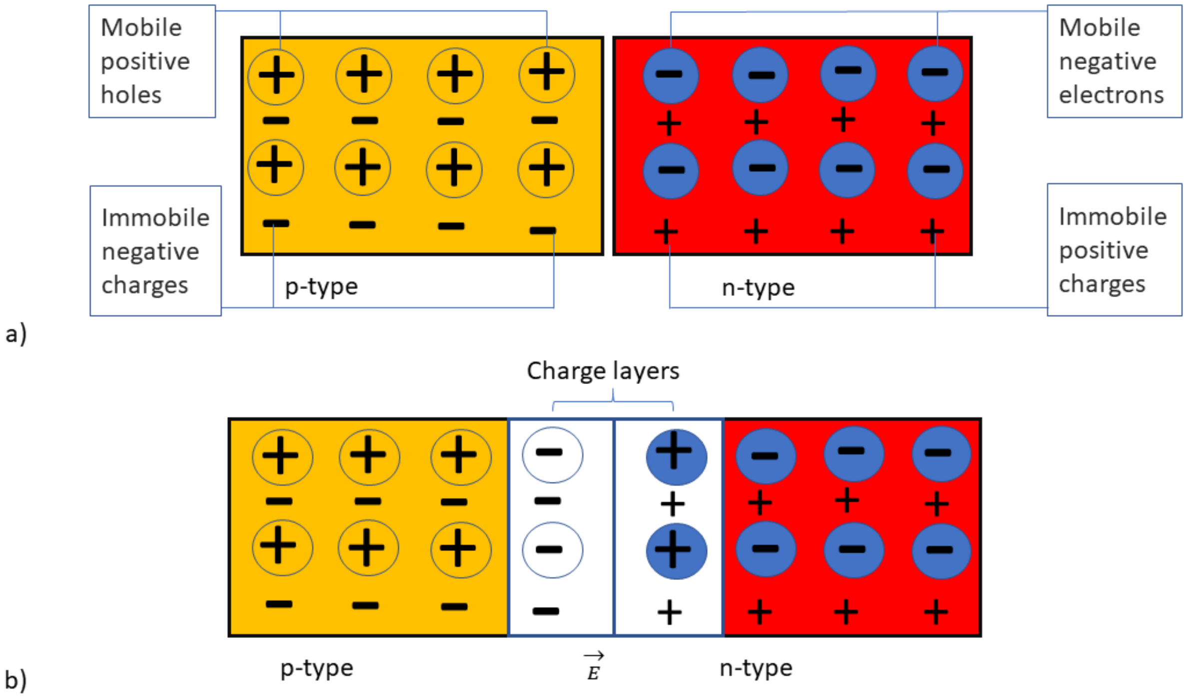

Figure 5: a)Extrinsic semiconductors, b) The formation of space charge region when p-type and n-type materials are brought together.

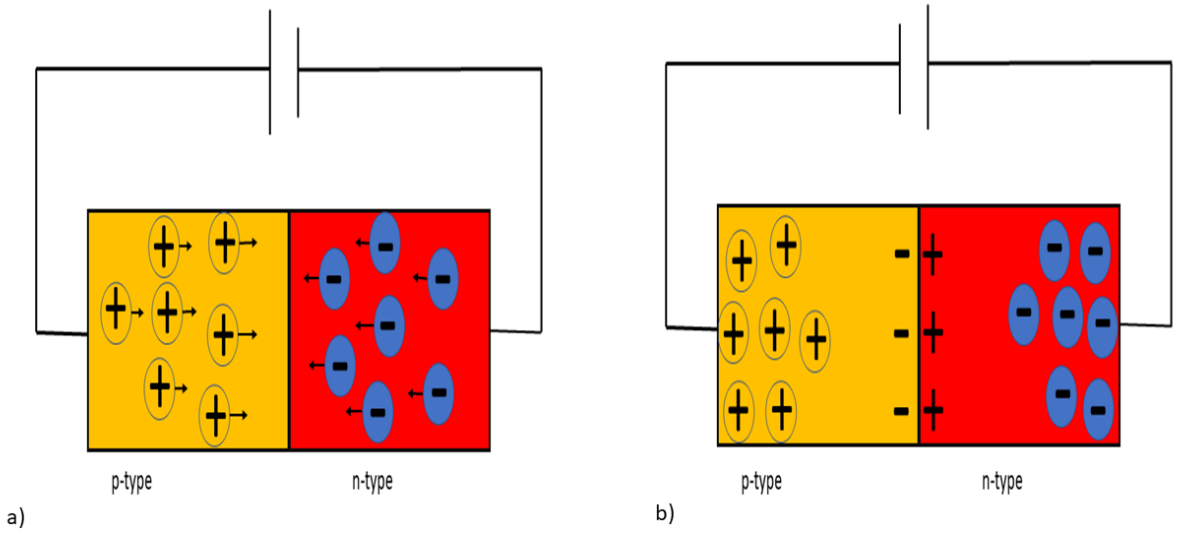

Figure 6: a) Forward bias, b) Reverse bias.

toward the depletion region as a result the depletion region and the potential barrier will reduce, allowing the charges to pass across this region (See Figure 6a). The voltage-current density characteristics can be derived from a model known as **ideal Schottky diode** and by using the **equivalent circuit model**

2.3 Ideal Schottky diode

We recall that in the forward bias condition, the electric field is reduced, and the drift current will be reduced too since it depends on it. Therefore the diffusion current is dominant over the drift current hence it is used to obtain the ideal diode equation given by

$$J = -J_o \left[exp \left(\frac{eV}{nk_B T} \right) - 1 \right] \tag{21}$$

Where the J_0 is the reverse saturation current density defined as:

$$J_0 = e \left(\frac{D_p}{L_p} \frac{n_i^2}{N_D^+} + \frac{D_n}{L_n} \frac{n_i^2}{N_A^-} \right) \tag{22}$$

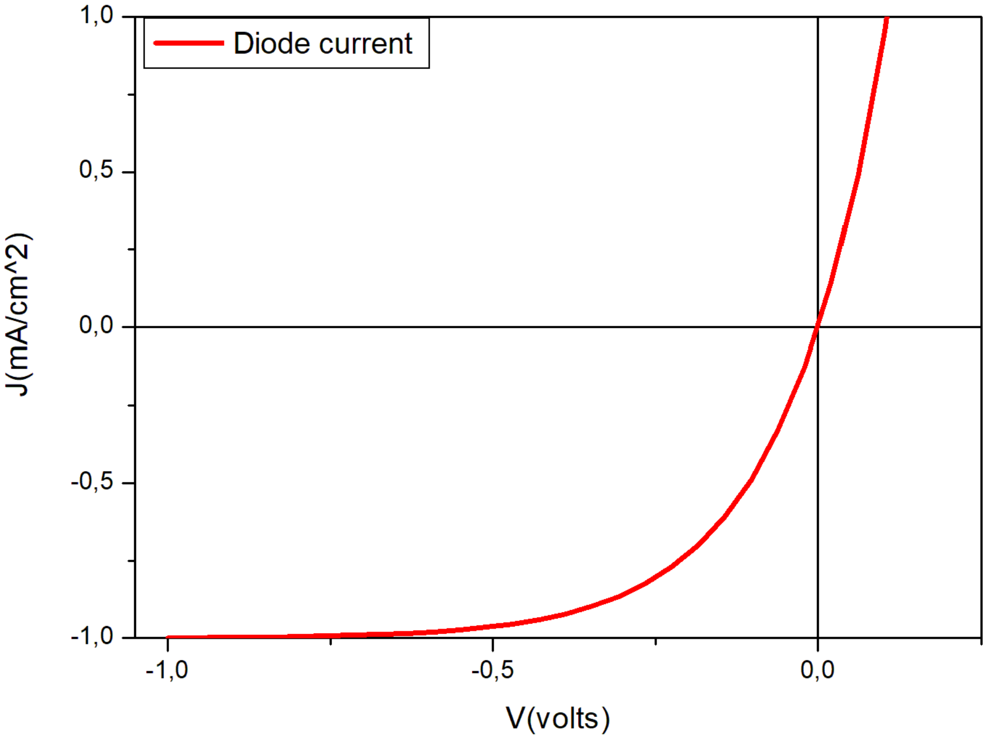

Figure 7: The typical diode J-V curve.

When the diode is irradiated with light electrons will be excited, resulting in the photo-generated current(J_{ph}). The output current is now given by the sum of the photogenerated current and the diode current.

$$J = J_{ph} - J_o \left[exp\left(\frac{eV}{nk_BT}\right) - 1 \right] \tag{23}$$

The real solar cell can be modeled by the equivalent circuit.

2.4 Equivalent circuit model

The ideal structure of a solar cell contains no series resistance and shunt resistance, but in reality, the ideal solar cell does not exist. The real solar cell has series resistance and shunt(parallel) resistance, and its structure is shown in Figure 8

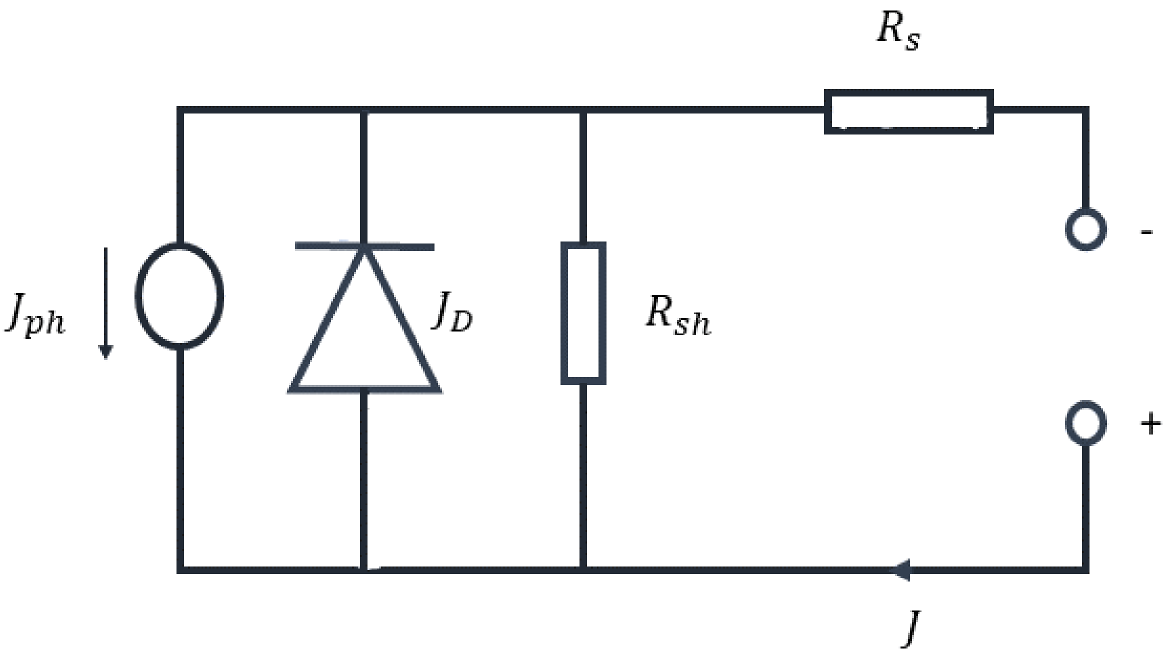

Figure 8: The equivalent solar cell circuit.

The shunt current density is given by

$$J_{sh} = \frac{V + JR_s}{R_{sh}} \tag{24}$$

The output current is given by the modified Schottky current which includes series resistance R_s and shunt resistance R_{sh}

$$J = J_{ph} - J_D - J_{sh} \tag{25}$$

$$J = J_{ph} - J_0 \left[exp(\frac{e(V + JR_s)}{nk_BT} - 1 \right] - \frac{V + JR_s}{R_{sh}} \tag{26}$$

The applied voltage can be derived from eq.23

$$V = \frac{nk_BT}{e} \ln \left(\frac{J_{ph} - J}{J_0} + 1 \right) \tag{27}$$

Where n and k_BT are ideality factor and Thermal energy respectively

2.5 Solar cell characteristics parameters

The general solar cell parameters that determine the performance of the solar cell are(shown in Figure 9): Short circuit current density J_{sc}, Open circuit Voltage V_{oc}, Fill Factor FF, External Quantum efficiency EQE, and Power conversion Efficiency PCE. The maximum

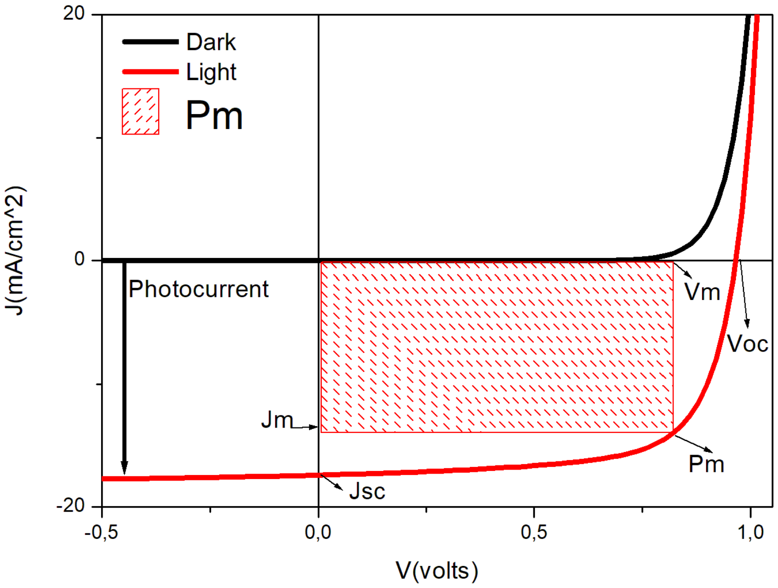

Figure 9: The typical J-V curve of a solar cell.

power a solar cell can produce is the product of the maximum voltage and maximum current density.

$$P_m = V_m J_m \tag{28}$$

The FF is the ratio of the maximum power to the product of the V$_{oc}$ and J$_{sc}$ given by the following equation

$$FF = \frac{J_m V_m}{J_{sc} V_{oc}} \tag{29}$$

The series resistance can be found by taking the derivative of the current density and equating it to zero when the current density is maximum. The derivative of eq.26 is therefore given by(for simplicity the shunt current is ignored)

$$\frac{dJ}{dV} = \frac{dJ_{ph}}{dV} - J_0 \frac{d}{dV}\left[exp(\frac{e(V+JR_s)}{nk_BT} - 1\right] = 0 \tag{30}$$

The first term in eq.30 is zero since the photo-generated current does not depend on the applied voltage, therefore eq.30 reduces to

$$\frac{dJ}{dV} = -J_0 \left(exp(\frac{e(V+JR_s)}{nk_BT}\right)\left[\frac{1}{nk_BT} + \frac{R_s}{nk_BT}\frac{dJ}{dV}\right] = 0 \tag{31}$$

For eq.31 to be zero the term inside the square brackets must be zero since the one inside the round brackets can not be zero.

$$\left[\frac{1}{nk_BT} + \frac{R_s}{nk_BT}\frac{dJ}{dV}\right] = 0 \tag{32}$$

$$\frac{1}{nK_BT}\left[1 + R_s\frac{dJ}{dV}\right] = 1 + R_s\frac{dJ}{dV} = 0 \rightarrow -\frac{1}{R_s} = \frac{dV}{dJ} \tag{33}$$

Therefore

$$R_s = -\left.\frac{dJ}{dV}\right|_{V_{0C}} \tag{34}$$

One can also write the shunt resistance as

$$R_{sh} = -\left.\frac{dJ}{dV}\right|_{J_{sc}} \tag{35}$$

The open circuit voltage is the voltage when there is no current in the circuit, which can be derived from eq.23 or eq.27, by setting J=0 and V=V$_{oc}$

$$V_{oc} = \frac{nk_BT}{e}\ln\left(\frac{J_{ph}}{J_0}+1\right) \approx \frac{nk_BT}{e}\ln\left(\frac{J_{ph}}{J_0}\right) \tag{36}$$

The Short circuit current density is the current when there is no external voltage applied on the circuit, which can be derived from eq.23 by setting V= 0 and J=J$_{sc}$ which leads to J$_{sc}$=J$_{ph}$. The PCE describes the amount of power converted by the solar cell from the irradiance of (1000W/cm^2) to electricity.

$$PCE = \frac{P_{out}}{P_{in}} = \frac{J_{sc}V_{oc}FF}{P_{in}} \tag{37}$$

As it can be seen from eq.37, the efficiency of the cell depends explicitly on the J$_{sc}$, V$_{oc}$, and FF

2.6 Charge transport in solar cells

2.6.1 Space charge limited current

The theory of space-charge-limited current between plane parallel electrodes is crucial in determining the charge carrier mobility. In the absence of light(under dark conditions) and traps the current density is given by the Mott-Gurney law [9, 29, 30, 31, 77]

$$J = \frac{9}{8}\mu\varepsilon\varepsilon_0\frac{V^2}{L^3} \tag{38}$$

Where μ is the field dependent mobility, ε_0 is the permittivity of free space,ε is the relative dielectric permittivity of the material, L denotes the thickness of the photoactive layer, and V is the voltage drop across the sample. For the set of a single set of traps, eqs.38 can be modified as follows

$$J = \frac{9}{8}\mu\varepsilon\varepsilon_0\frac{V^2}{L^3}\theta_0 \tag{39}$$

Where θ_0 is given by the following relation

$$\frac{\rho_f}{\rho_f + \rho_t} = \theta = \frac{N_c}{N_t} \exp\left(-\frac{A}{KT}\right) \tag{40}$$

Where ρ_f and ρ_t are the free and trapped charge densities, and N$_c$ and N$_t$ are the effective conduction band density of states, and density of traps respectively. The current density is given by.

$$J = \mu \rho_f E \tag{41}$$

With the contribution of the diffusion current being neglected. substituting eq.40 into eq.41 we get

$$J = \theta_0 \mu (\rho_f + \rho_t) E \tag{42}$$

Taking the relationship of the electric field with the charge density, given by Poisson's equation

$$\frac{dE}{dx} = \frac{\rho_f + \rho_t}{\varepsilon \varepsilon_0} \tag{43}$$

Eq.42 reduces to

$$J = \theta_0 \mu \varepsilon \varepsilon_0 E \frac{dE}{dx} \tag{44}$$

Eq.44 can be integrated as follows

$$J \int_0^x dx = \theta_0 \mu \varepsilon \varepsilon_0 \int_{E(0)}^{E(x)} E dE \tag{45}$$

$$Jx = \theta_0 \mu \varepsilon \varepsilon_0 \frac{E^2(x) - E^2(0)}{2} \tag{46}$$

If the injecting electrode is at x=O, E(0) is assumed to be zero and

$$E(x) = \left(\frac{2Jx}{\theta_0 \mu \varepsilon \varepsilon_0}\right)^{\frac{1}{2}} \tag{47}$$

The voltage V dropped across the sample can be determined by integrating eq.47 over the absorber layer thickness L as follows

$$V = E\int_0^L dx = \left(\frac{2J}{\theta_0\mu\varepsilon\varepsilon_0}\right)^{\frac{1}{2}}\int_0^L x^{\frac{1}{2}}dx \tag{48}$$

$$EL = \frac{2}{3}\left(\frac{2J}{\theta_0\mu\varepsilon\varepsilon_0}\right)^{\frac{1}{2}} L^{\frac{3}{2}} \tag{49}$$

And the current density J can be obtained by rearranging eq.49

$$J = \frac{9}{8}\theta_0\mu\varepsilon\varepsilon_0\frac{E^2}{L} \tag{50}$$

According to Frenkel(1938), the effective depth of traps may be reduced by the presence of a strong electric field, this was later discussed by Verimilyea(1954). The charge current density -voltage equation due to the Frenkel effect is defined as(the full derivation can be found in ref [29])

$$J = \frac{9}{8}\theta_0\varepsilon\varepsilon_0\mu\exp\left(\frac{0.89}{K_BT}\sqrt{\frac{e^3V}{\pi\varepsilon\varepsilon_0L}}\right)\frac{V^2}{L^3} \tag{51}$$

2.7 Organic solar cell

Organic solar cells/organic photovoltaic solar cells are devices that convert sunlight energy into electrical energy by using conducting polymers. These polymers offer both the absorption and conducting properties of a semiconductor. Many optoelectronic devices have been made from these polymers such as light emitting diodes, bio-sensors, touch screens, supercapacitors, photovoltaics, etc [49]. These polymers have gained extensive attention owing to their superior advantages such as the ability to tailor their electrical and optical properties through structural modifications, ease of synthesis, flexibility, cheap production cost, and ease of processability [33, 37, 50]. The conducting property of polymers can be explained by the bonds that exist between the Caborn atom and neighboring atoms in the polyacetylene [49]. In polyacetylene, carbon atoms in the polymer main chain are sp2 hybridized and each carbon atom forms three covalent sigma-bonds with adjacent neighboring atoms, The 2pz unhybridized orbital overlaps with the other unhybridized 2pz orbital of the neighboring carbon atom, leading to the delocalization [10, 12, 33, 37, 46, 51] of the electrons forming the π band. This half-filled π band would make the polymer-metal, nevertheless, the structure dimerizes due to Peierls instability [49, 54], forming a completely occupied π band and an empty π^* band, which gives conjugated polymers their semiconducting characteristics. The energy band formation can be realized in Figure 10, where the conjugation of molecules results in the splitting of energy levels for instance, the conjugation in Figure 10 starts with ethene, and one of the carbons is single-bonded into the ethene to form butadiene. If this chain keeps repeating

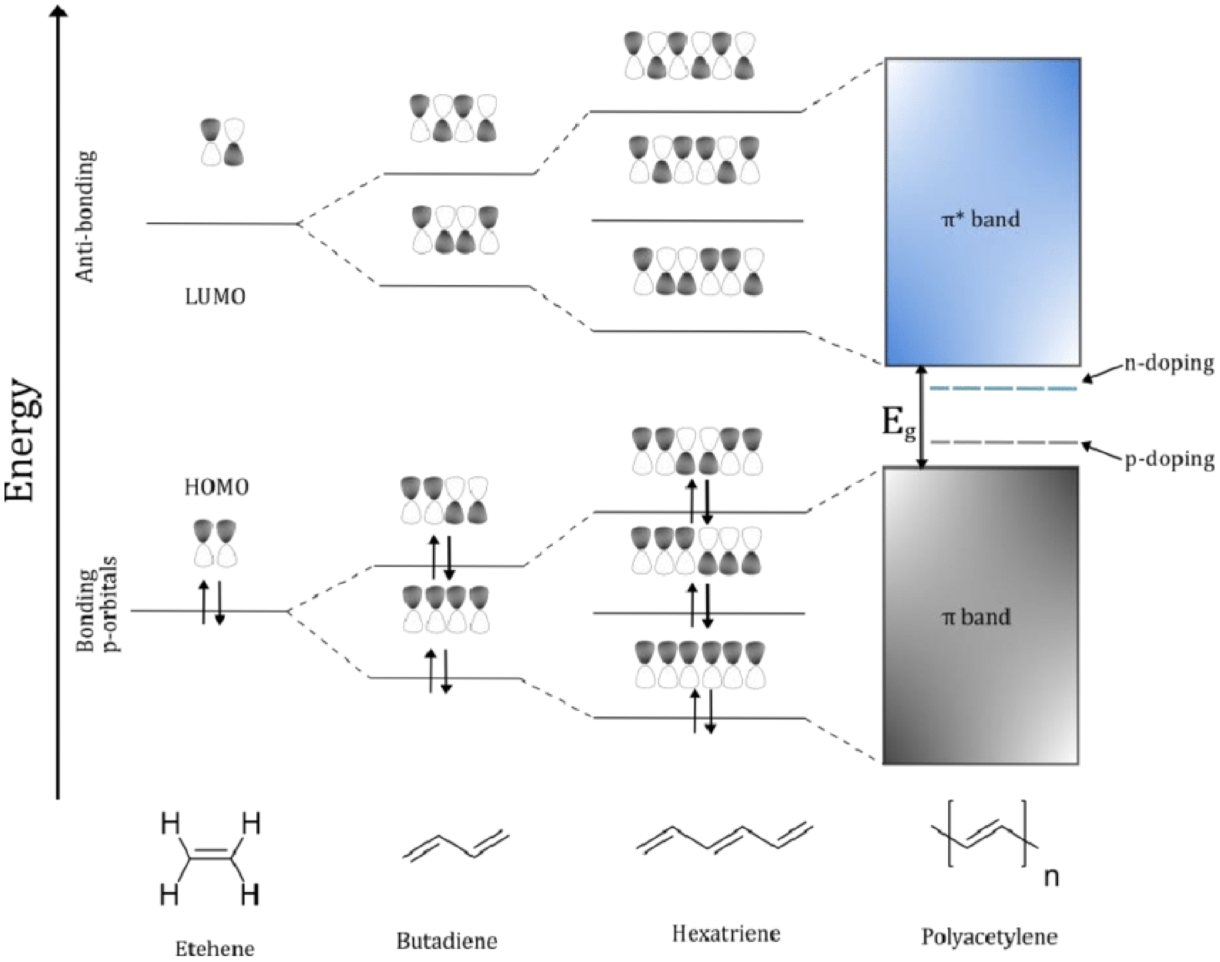

Figure 10: Increasing the conjugated chain length introduces new energy states of the π-bonds orbital conformations and in turn decreases the band gap. In a hypothetical infinitely long polyacetylene chain, these levels will start to blend and form seamless bands. By doping the material can extra energy levels of electrons and holes be introduced into the material, making it more conductive. this figure and the caption were taken from ref [56].

Hexatriene will be formed, then polyacetylene with more splitting in the energy levels leading to the formation of π and π^* bands, also known as the highest occupied molecular orbital(HOMO) and lowest unoccupied molecular orbital(LUMO) respectively [37]. The OSCs are continuously designed based on these polymers, some of the chemical structures of the materials used to design OSCs are shown in Figure 11. Although OSCs have made such progress, they still differ from their counterparts inorganic solar cells due to the physical parameters that characterize them such as mobilities, energy band gap, dielectric constant, Coulomb forces, etc. Inorganic semiconductors such as Silicon have narrow energy band gaps of $1.1eV$ [35]. which is an indirect band gap meaning that the crystal momentum of electrons and holes remains the same in the conduction band and the valence band and an electron can directly emit a photon. The excitation in the silicon

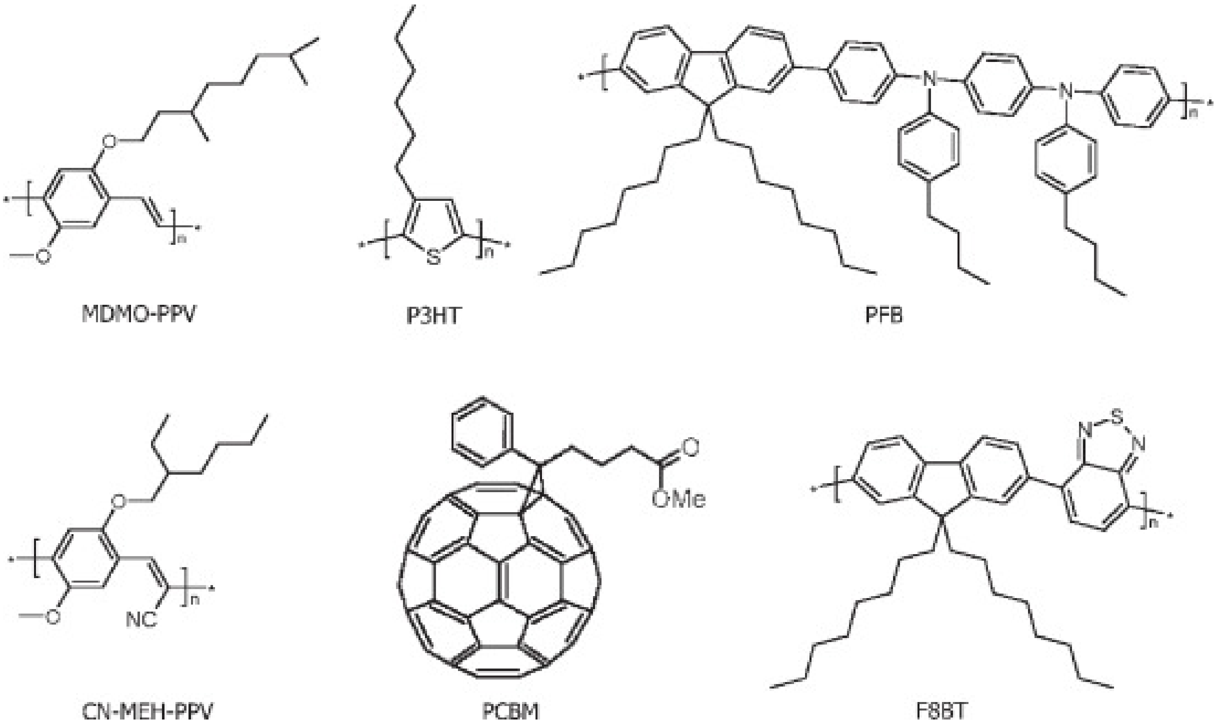

Figure 11: Chemical structures of some of the most common organic materials used in the fabrication of OSCs. Upper row: the p-type hole conducting donor polymers MDMO-PPV (poly[2-methoxy-5-(3,7- dimethyloctyloxy)]-1,4-phenylen evinylene), P3HT (poly(3-hexylthiophene2,5-diyl) and PFB (poly(9,9'-dioctylflu orene-co-bis-N,N'-(4-butylphenyl)-bisN,N'-phenyl-1,4-phenylenediamine). Lower row: the electron conducting acceptor polymers CN-MEH-PPV (poly-[2-methoxy-5-(2'-ethylhexyloxy)- -1,4-(1-cyanovinylene)-phenylene) and F8TB (poly(9,9'-dioctylfluoreneco- -benzothiadiazole) and a soluble derivative of C60, PCBM (1-(3- methoxycarbonyl) propyl-1-phenyl[6,6]C61). Figure taken from ref [37].

semiconductor by the electromagnetic energy results in the generation of free charges, which can be collected immediately after being generated this is due to the large dielectric constant $\varepsilon_r = 11$ leading to weak coulomb forces and small binding energy. In the absence of external energy, these free charges can also be created by thermal excitation (at room temperature) from the valence band to a conduction band, with a concentration of charge carriers given by N = $\mathrm{N}_{eff}e^{-E_g/2KT}$, where N_{eff} is the effective density of valence or conduction band states and Eg is the band gap [12]. These materials have intrinsic conductivities ranges from 10^{-8} to 10^{-2} Ω^{-1} cm^{-1} [12]. Contrarily, the conductivity of organic semiconductors is extrinsic and is brought about by the injection of charges at electrodes, by purposeful or accidental doping, and by the dissociation of photo-generated electron-hole pairs that are bonded by their mutual coulomb attraction. The energy band gap of organic semiconductors is wide in the range of 1 eV−3 eV, which can be direct or indirect, and they have a small dielectric constant of $\varepsilon_r = 3.5$ [40, 44, 53, 55] leading to large coulomb forces and binding energy [12, 34, 46] of $0.5eV - 1eV$, which limit the creation of free charges by thermal excitation, and therefore more energy is required to overcome the coulomb force. Lastly the V_{oc} in organic solar cells is defined as the energy difference between the energy of the LUMO of the acceptor material and the HOMO of the donor material [36, 42, 44, 55]

$$V_{oc} = \frac{1}{q}\left({E_{LUMO}}^{A} - {E_{HOMO}}^{D}\right) - 0.3 \tag{52}$$

where A and D stand for acceptor and Donor respectively,the value of 0.3 V in eq.66 is an empirical factor which is related to the coulomb attraction between holes and electron [44]

2.8 Working principle of organic solar cells

2.8.1 Absorption and exciton generation

Compared to Traditional silicon solar cells, organic solar cells cannot produce free charges without external energy. The absorber material absorbs photon energy to generate free charges. Due to high binding energy EB $>$ 0.3 eV, bound excitons are created rather than free charges. The photon energy must be greater than the energy difference (band gap) HOMO and LUMO of the absorber material, for the electrons to be excited from HOMO to LUMO, leaving a hole behind. The photon absorption efficiency for any material $\eta_{PA}(\lambda)$ [1, 55] depends on the absorption coefficient of the absorber molecule, transmitted photons whereas the reflected photons are lost [1]. Additionally, the absorber layer thickness (which is in the range of the coherence length of the sunlight) and its position within the optical field distribution created by interference determine $\eta_{PA}(\hbar\omega)$. Hence, an optimization of η_{PA} means finding molecules with high absorption in the desired spectral range and optimizing the stack regarding optics [1]. The absorber material absorbed the light energy hv which generated bound excitons, the binding energy is EB $>$ 0.3eV which poses difficulty in separating the generated excitons. For separation, the exciton has to undergo diffusion.

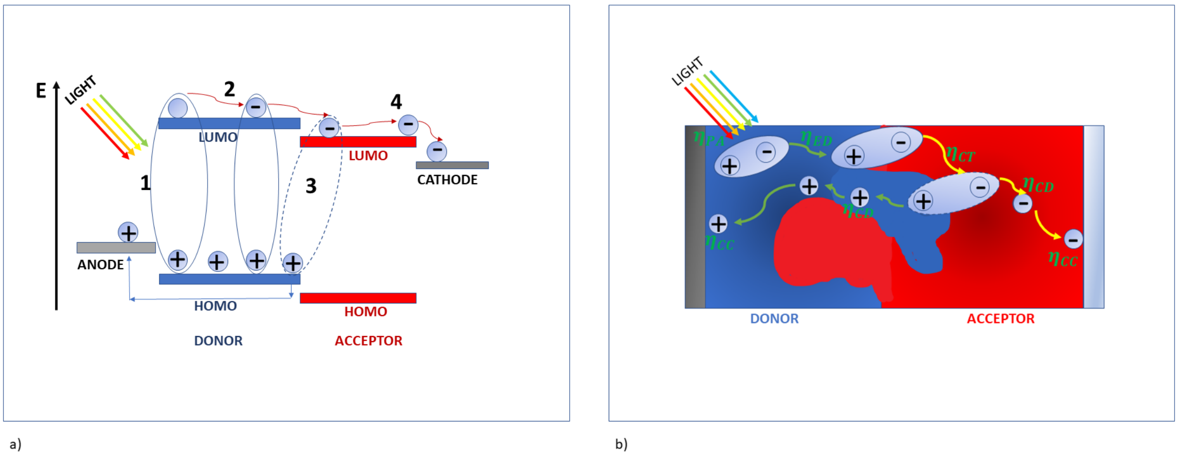

Figure 12: a) Four steps governing the operating mechanism of OSCs in the energy diagram, 1) Absorption and exciton generation,2) Exciton diffusion,3) Exciton dissociation, and 4)Charge transport and charge collection. b) The working principle showed in the blended materials that represent a Bulk-heterojunction structure.

2.8.2 Exciton diffusion

The generated electric field plays a very important role in separating the electron-hole pairs, as already stated in organic solar cells the generated charges are bound together, unlike in inorganic solar cells where free charges are created immediately, and diffuse across the junction and can be collected by the electrodes. The excitons in organic solar cells diffuse towards the interface where they get separated by the electric field, hence the drift current is dominant over the diffusion current in organic solar cells. These excitons have to travel a certain distance to reach the interface, this distance is known as the diffusion length ($L_D = \sqrt{D\tau}$) which is limited to 10 nm [35, 38, 39, 40, 46, 48]. The diffusion efficiency η_{ED} is given by the ratio of the diffusion length to the thickness of the absorber layer[1, 55]. if the excitons are generated outside this distance, recombination will occur, however BHJ was developed such that excitons are generated within the diffusion length [45].

2.8.3 Charge transfer

As the exciton diffuses to the interface, the charge transfer will occur at the interface such that the electron will be transferred from the LUMO of the donor material to the LUMO of the acceptor material, and the holes from the HOMO of the acceptor material to the HOMO of the donor materials. These charges might or might not be still bound by the intermolecular force. The charge transfer efficiency η_{CT}[55] requires an offset in the electron affinities (ionization potentials) for electron (hole) transfer between donor and acceptor, which is larger than the exciton binding energy [1].

2.8.4 Exciton dissociation

It is not clear whether the dissociation of exciton occurs during the charge transfer process or whether the energy gained from the energy level offset is used to directly generate free charge carriers via hot excitons. The full explanation of the proposals that may lead to charge dissociation and its efficiency η_{CD} can be found in reference [1].

2.8.5 Charge transport and charge collection

After dissociation electrons will be transported by the accepter material and holes will be transported by the donor material to the respective electrodes. The efficiency of charge transport η_{CP}[1, 55] may only be affected by the recombination (non-germinate) of electrons and holes leading to the loss of charges. Finally, the electrons will be collected by the cathode and holes will be collected by the anode. The efficiency of charge collection is given by η_{CC} [1, 55]. The summary of the working principle of OSCs is shown in Figure 12. The above discussed efficiencies can be used in determining the External Quantum Efficiency (EQE)

2.8.6 External quantum efficiency

The product of the discussed efficiencies yields the quantum efficiency, also known as the incident-photon to-electron conversion efficiency (IPCE) or external quantum efficiency (EQE) [1, 3, 43, 47, 55], as a function of temperature T, applied voltage V (which affects the electric field F), and wavelength λ. EQE is defined as:

$$\eta_{EQE} = \eta_{PA}\eta_{IQE} = \eta_{PA}\eta_{ED}\eta_{CT}\eta_{CD}\eta_{CP}\eta_{CC} \tag{53}$$

Where η_{IQE} is the internal quantum efficiency, defined as the ratio of carriers collected at an electrode to photons absorbed in the device. Eq.53 can be used to find the short current density, which is given by the following equation [38, 55]

$$J_{sc} = \frac{q}{\hbar c}\int_{\lambda_{min}}^{\lambda_{max}} EQEP_{in}(\lambda)\lambda d\lambda \tag{54}$$

Chapter 3

3 Absorption enhancement methods for solar cells

Light harvesting materials are in high demand owing to the abundant energy coming from the sun which most of it is not utilized. Currently, OSCs are only capable of converting less than 21 % of the photon energy, which is very small compared to the amount of energy consumed globally each year. However, the incorporation of nanostructures such as nanoparticles, nanorods, nanoshells, and nanowires in solar cells is gaining popularity due to unique optical properties offered by these nanostructures, such as strong interaction with the light because of the occurrence of LSPR. Among the most widely used metal nanoparticles are those of nickel and cobalt, which have several uses in a variety of fields, such as photovoltaics as light traps, water purification, medicine, and chemical reactions as catalysts. In this work, Bi-MNPs are mixed i the charge transport (PEDOT:PSS) to influence positively the charge collection mechanisms in OSC.

3.1 Plasmon nanoparticles assisted light trapping in OSC

The inclusion of nanoparticles in the OSC device has demonstrated improvement in the device's light absorption, and charge transport processes that enhance the collection of photogenerated current [59]. Depending on their position in the device, MNPs play a vital role in guiding the light within the OSC device. for example, the unabsorbed light can be guided to the region of maximum cell absorption through scattering. LSPR occurs through the interaction of the incident light with the surface electrons of the metal nanoparticles. The electric field component of the incident light polarizes the surface electron concentration which induces a dipole moment that oscillates with time. (as shown in Figure 13a). The occurrence of LSPR is dependent on the size, shape, position, and geometry of nano-material [58, 59, 63, 65, 66, 67, 68]. The LSPR decays into various channels, which include energy transfer into the vinical semiconductor. The energy transfer processes can be split into two main parts: Radiative and non-radiative energy transfer [57]. The non-radiative decay leads to the generation of hot electrons and plasmon-induced resonance energy transfer(PIRET). Plasmonic metal nanoparticles absorb light that leads to the generation of hot electrons [57]. These electrons can be used to generate current when they cross the potential barrier in the metal-semiconductor and enter the conduction band. In the case of PIRET, sunlight is absorbed by the plasmonic metal nanoparticle, which then uses dipole-dipole coupling to transfer the energy from a metal to a semiconductor, leading to the creation of electron-hole pairs below and close to the semiconductor band edge [58]. Radiative energy transfer is a critical property of the plasmonic nanoparticle because it influences the semiconductor's light absorption. To describe radiative energy transfers, two basic components can be used: near-field coupling (absorption) and far-field scattering. In both scenarios, the plasmonic nanoparticles serve as secondary energy sources [57]. For example, in the NEAR field coupling, the small-sized plasmonic metal nanoparticle absorbs light and emits it, causing the emitted photons to be absorbed by the vicinal semiconductor. The light is scattered by the large plasmonic nanoparticle [58] until it is absorbed by the nearby semiconductor. Therefore, Due to LSPR excitations, the optical cross-section extinction σ_e is improved which is given by the combination of the scattering cross-section and absorption cross-section.

$$\sigma_{ext} = \sigma_{abs} + \sigma_{scatt} \tag{55}$$

The scattering and absorption cross sections for spherical nanoparticles were first found by Gustav Mie in the early 1900s. The scattering and absorption extinction cross-sections are defined as [57, 58, 60, 62, 65]:

$$\sigma_{abs} = \frac{24\pi^2 r^3 \varepsilon_m^{\frac{3}{2}}}{\lambda} \frac{\varepsilon_i}{|\varepsilon + 2\varepsilon_m|^2} \tag{56}$$

$$\sigma_{scatt} = \frac{32\pi^4 r^6 {\varepsilon_m}^2}{\lambda^4} \left| \frac{\varepsilon - \varepsilon_m}{\varepsilon + 2\varepsilon_m} \right|^2 \tag{57}$$

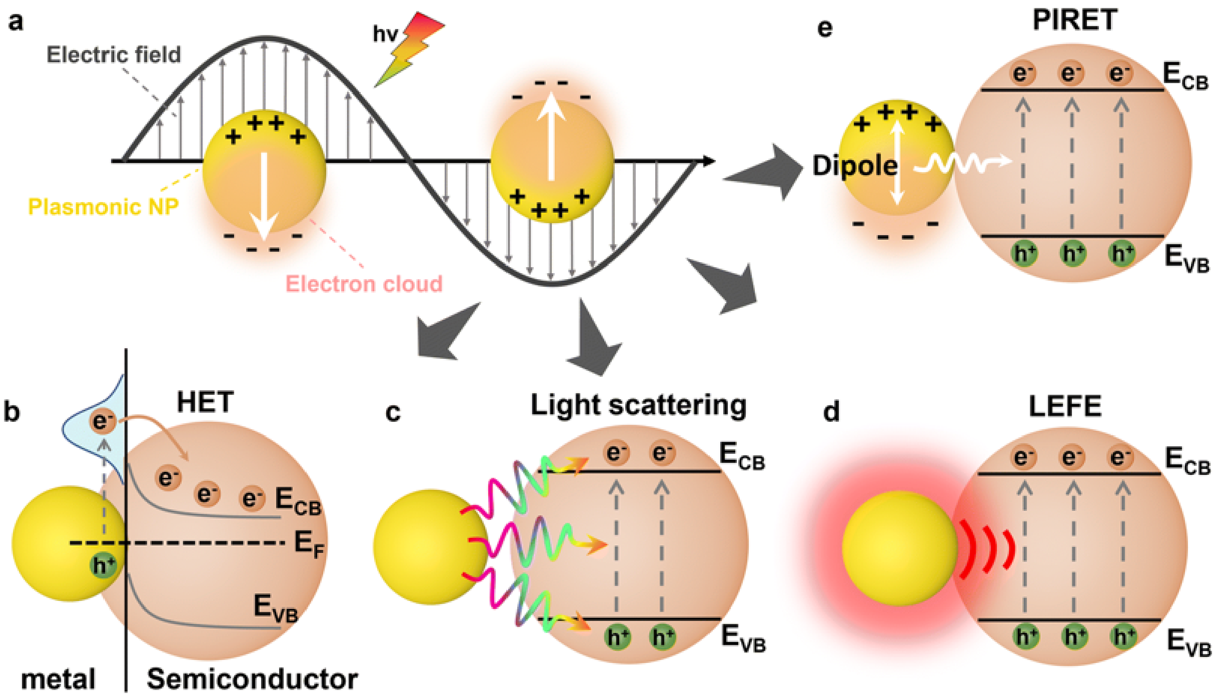

Figure 13: The LSPR excitation effect: a) LSPR, b) generation of hot electrons,c) far-field-scattering, d)near-field-coupling,e) Plasmon Induced resonance energy transfer, the picture and caption were taken from ref [58].

Where ε and ε_m are the complex permittivity of the metal and permittivity of the surrounding material which are very important in determining the resonance condition of light with the nanoparticle.

3.1.1 Plasmon resonance frequency

The permittivity is one of the physical parameters that describe the optical properties of the metal nanoparticles. The permittivity is made of both real and imaginary parts and is given below

$$\varepsilon(\omega) = \varepsilon_r(\omega) + i\varepsilon_i(\omega) \tag{58}$$

where ω is the angular frequency, the real part determines the position of the resonance and the imaginary part determines the dephasing. Considering conduction electrons to be free, the Drude model is used to describe the permittivity of the metal[62, 65]

$$\varepsilon(\omega) = 1 - \frac{\omega_p^2}{\omega(\omega + i\gamma_b)} \tag{59}$$

Where ω_p and γ_b are the plasma frequency and the bulk damping constant given by[60]

$$\omega_p = \sqrt{\frac{e^2 n}{\varepsilon_0 m}} \tag{60}$$

$$\gamma_b = \frac{\nu_F}{l_m} \tag{61}$$

Where ν_F and lm are the Fermi velocity and mean free path respectively. The temporal length of damping (given by the product of $\omega\tau$, where τ is the free electron gas's relaxation period) is substantially larger than unity at frequencies close to ω_p, it is approximated that the damping is negligible. Therefore, by discarding the damping term from eq.59 [62]

$$\varepsilon(\omega) = 1 - \frac{\omega_p^2}{\omega^2} \tag{62}$$

It is clear that from eq.56 and eq.57, the strong interaction of the nanoparticle occurs when the imaginary part of ε is close to zero, and $\varepsilon = -2\varepsilon_m$ which leads to the occurrence of LSPR [60, 61, 62, 63, 64, 65]. In the dipole approximation, the peak or maximum frequency is given by [60, 62]

$$\omega_{max} = \frac{\omega_p}{\sqrt{2\varepsilon_m + 1}} \tag{63}$$

Chapter 4

4 Device structure and preparation of OSCs

4.1 Experimental

The device structure of thin film organic solar cell is composed of solar absorber layer, charge transport layers, and electrodes. Indium tin oxide(ITO) coated glass, is a frequently used anode in the preparation of thin film organic solar cells in the laboratory scale. It has a transmittance of around 90 % and is transparent and non-reflective. Because of their high work function and ability to reflect light, cathodes such as silver and aluminum are frequently employed in organic solar cells (OSCs). Figure 14 depicts the OSC conventional device structure. The active layer comprises two polymer molecules such as donor and acceptor material blended in an appropriate solvent to form a solution. The solution is then spin coated on the substrate and sandwiched between the electrodes. Additionally, buffer layers are added between the electrodes to improve charge transport

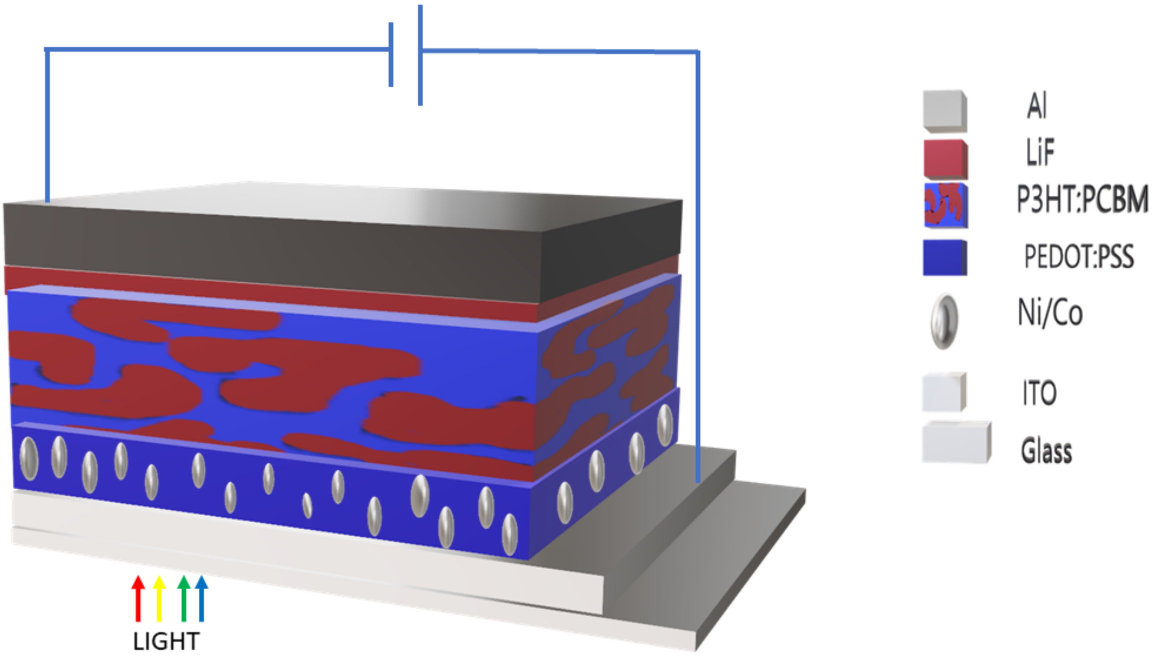

Figure 14: basic structure of the OSC cell device with Ni/Co Nps added in the PEDOT:PSS buffer layer.

and prevention of surface recombination. PEDOT: PSS is used as the hole transport layer(HTL) inserted between the anode and the active layer. HTL blocks the electrons from flowing to the anode allowing only the holes. LiF is used as the electron transport layer(ETL) inserted between the cathode and the active layer. ETL blocks the holes from flowing to the cathode allowing only the electrons.

4.1.1 Synthesis of Ni/Co BMNPs

The chemical reduction method was employed to synthesize Ni/Co BMNPs. The required chemicals were 40 mM of nickel nitrate 20 mM of cobalt nitrate and 0.1 M of Sodium borohydride used as the reducing agent in the aqueous solution. Two separate solutions were prepared from 40 mM of $Ni(N0_3)_2$, to 20 mM of $Co(N0_3)_2$, respectively, in 25 mL of distilled water and each containing 0.1 M of $NaBH_4$. The solutions underwent a productive agitation at ambient temperature and were safely amalgamated through a meticulous dropwise addition technique while the mixture was stirred continuously. After 3 hrs of stirring on a hot plate at 40 °C, the amalgam needed some purification. The mixture underwent filtration and was thoroughly rinsed with distilled water to extract any lingering sodium ions. The end result was a suspension that was devoid of any undesirable particles. The Ni/Co BMNPs precipitate was left to dry for 2 hrs in a vacuum oven set to 70 °C. This ensured the amalgam would be moisture-free, making it a highly desirable end product.

4.1.2 Device preparation

The ITO-coated glass substrates were used as received from the suppliers, which is of the size 20 mm x 15 mm and sheet resistance of 10 Ω/sq. The ITO was partially etched with an acid solution, It was then cleaned with detergent, acetone, and ethanol, and it was rinsed with distilled water. The substrate was then sonicated with de-ionized water, acetone, and isopropanol for 10 mins each. It was then transferred to the oven to be dried for 20 mins at 90 °C. followed by the **Deposition PEDOT:PSS with Ni/Co** . In the PEDOT:PSS, Ni/Co was added at weight ratios of 0.0 %, 0.05%, 0.15 %, and

0.25 %. After that, the solutions were sonicated with magnetic stirring overnight to ensure a smooth mixture. The solutions were spin-coated on the substrates at 3500 rpm for 60 s. After that, the devices were placed in the oven to dry for 20 mins at 100 °C before **P3HT:PCBM depostion**. The photoactive layer solution was prepared from P3HT:PCBM blend in chloroform solvent. The 5 mg of P3HT and PCBM were measured using the weighing balance and were then dissolved with chloroform. The solution was placed on the hot plate 3 hrs for stirring to obtain good miscibility. The P3HT:PCBM solution was dispersed on the spinning PEDOT: PSS-covered substrate at the speed of 1200 rpm for 40 s. The devices were then transferred into the furnace under a nitrogen atmosphere to dry for 10 mins at 90 °C, followed by the **LiF and Al deposition**. The devices were transferred into a vacuum deposition chamber(Edwards Auto 306) for the deposition of lithium fluoride (LiF) and aluminum (Al). LiF was evaporated first and a thickness of 0.5 nm was achieved followed by the the evaporation of Al with a thickness of 80 nm being achieved. The materials were evaporated at a pressure of $1.9\text{x}10^{-6}$ mbar, after that, the devices were transferred into the furnace under a nitrogen atmosphere to dry for 10 mins at 90 °C. The J –V data were taken using the Keithley Source meter. Light illumination was measured by solar simulator SS-50A at an intensity of 100 mW/cm^2. The optical absorption spectra were measured using a Perkin Elmer Lambda 9 Spectrophotometry.

4.2 Device simulation method

The fabricated solar cells are simulated by device simulation program called SCAPS(Solar cell capacitance simulator). SCAPS is a one-dimensional simulation program. The SCAPS program was developed at the Department of Electronics and Information Systems (ELIS) of the University of Gent Belgium[69, 70, 71, 72]. The operation of SCAPs follows four steps depicted in Figure 15a, the front face of SCAPS is shown in Figure 16. The semiconductor layers such as those shown in Figure 14 can be added under definition panel layers one at a time, SCAPS is limited to only seven layers.

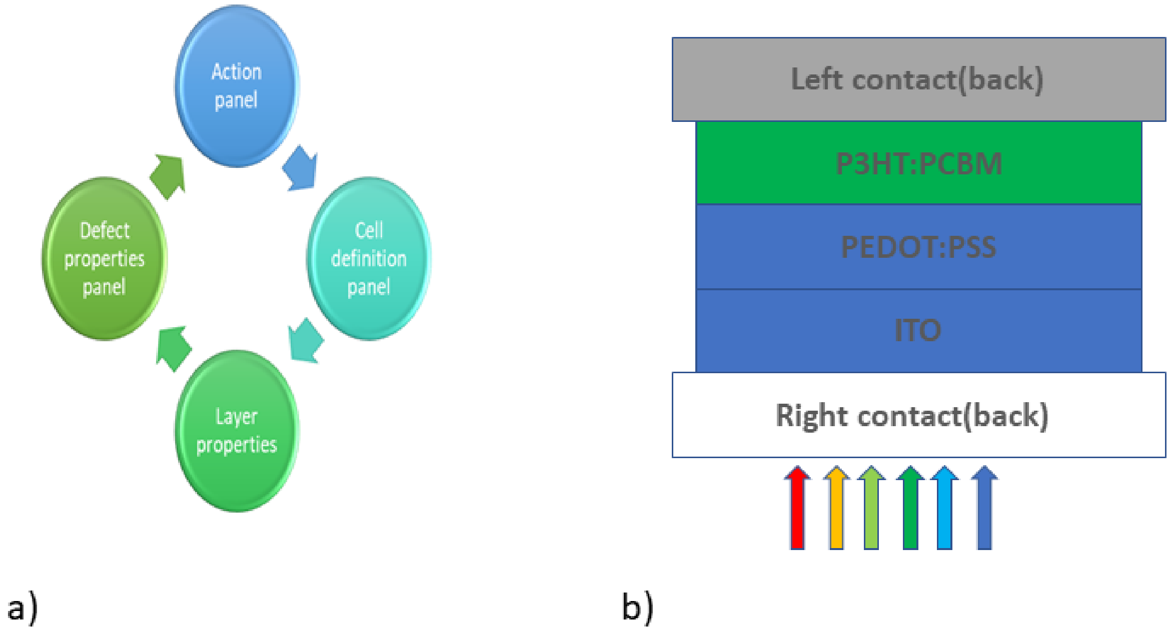

Figure 15: a) Four steps operation of SCAPS, b) OSC structure in SCAPS.

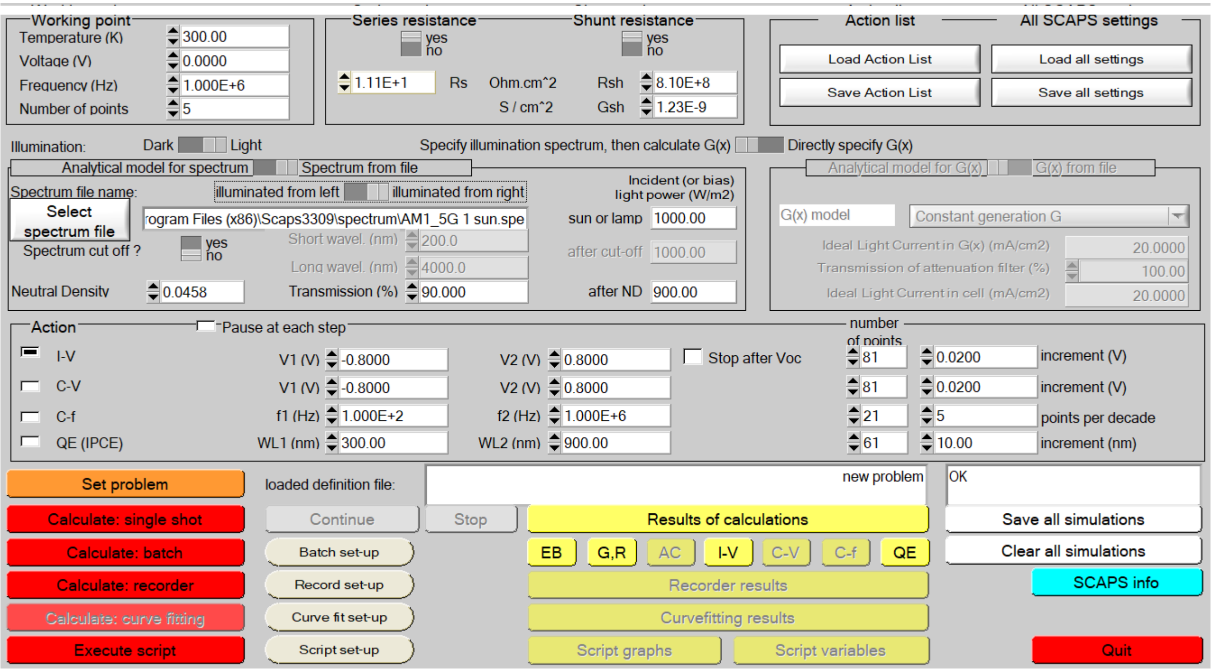

Temperature (K) 300.00
Voltage (V) 0.0000
Frequency (Hz) 1.000E+6
Number of points 5

Series resistance: yes / no; 1.11E+1 Rs Ohm.cm^2

Shunt resistance: yes / no; Rsh 8.10E+8; S / cm^2 Gsh 1.23E-9

Illumination: Dark / Light

Specify illumination spectrum, then calculate G(x) / Directly specify G(x)

Analytical model for spectrum / Spectrum from file

Analytical model for G(x) / G(x) from file

Spectrum file name: illuminated from left / illuminated from right

rogram Files (x86)\Scaps3309\spectrum\AM1_5G 1 sun.spe

Spectrum cut off ? yes / no

Short wavel. (nm) 200.0
Long wavel. (nm) 4000.0

Neutral Density 0.0458
Transmission (%) 90.000

Incident (or bias) light power (W/m2)
sun or lamp 1000.00
after cut-off 1000.00
after ND 900.00

G(x) model: Constant generation G
Ideal Light Current in G(x) (mA/cm2) 20.0000
Transmission of attenuation filter (%) 100.00
Ideal Light Current in cell (mA/cm2) 20.0000

Pause at each step

Action					number of points		
☑ I-V	V1 (V) -0.8000	V2 (V) 0.8000	☐ Stop after Voc		81	0.0200	increment (V)
☐ C-V	V1 (V) -0.8000	V2 (V) 0.8000			81	0.0200	increment (V)
☐ C-f	f1 (Hz) 1.000E+2	f2 (Hz) 1.000E+6			21	5	points per decade
☐ QE (IPCE)	WL1 (nm) 300.00	WL2 (nm) 900.00			61	10.00	increment (nm)

loaded definition file: new problem

OK

Figure 16: Action panel (SCAPS front face), This figure is a screenshot from the SCAPS software.

The software cannot simulate until physical parameters are provided for these layers. Under layer properties physical parameters such as Energy band gap (Eg), thickness, mobility, electron affinities, etc, must be added for each layer. Possible calculations such as current voltage, capacitance-voltage, capacitance-frequency, and quantum efficiency can be made under an action pane ,under dark conditions, or under illumination with the light spectrum of 1000W/cm^2. The full details of the operation of SCAPS can be found in the most recent SCAPS manual in ref [69]. The materials that were used in this study are shown in Figure 15b with no LiF, due to its large energy band gap which is beyond acceptable value in SCAPS, however, to account for this material, the electron affinity of the absorber layer was increased to 4.2 eV to match the work function of the Aluminium electrode so that they form an ohmic contact. The physical parameters for each layer are shown in Table 1 taken from our previous work in ref [81].

Table 1: simulation parameters FOR ITO, PEDOT:PSS hole transport layer(HTL), and P3HT:PCBM absorber layer(ABL)

Parameter	symbol	ITO	HTL	ABL	units
Thickness	d	80	45	180	nm
Energy band gap	E$_g$	3.6	2.2	-	eV
Electron affinity	χ	4.8	4.4	-	eV
Di-electric permittivity(relative)	ϵ	8.9	10	3.8	
CB effective density of states	N_C	1×10^{19}	3.6×10^{21}	1.8×10^{21}	cm^{-3}
VB effective density of states	N_V	1×10^{19}	4.1×10^{20}	5×10^{20}	cm^{-3}
electron thermal velocity	v	1×10^7	1×10^7	1×10^7	cm s^{-1}
hole thermal velocity	v	1×10^7	1×10^7	1×10^7	cm s^{-1}
electron mobility	μ_n	10	0.001	0.01	cm^2/Vs
hole mobility	μ_p	10	0.0001	0.001	cm^2/Vs
doping concentration of acceptors	N_A	1×10^{12}	1×10^{14}	0	cm^{-3}
doping concentration of Donors	N_D	1×10^{17}	-	0	cm^{-3}

4.3 Numerical device simulation

The SCAPS program uses a fundamental transport equation as defined below. The equations were solved numerically for different types of design. continuity equations for electrons and holes are given by eq.12 and eq.13 and the Poissons equation given by [69, 72]

$$\frac{\partial}{\partial x}\left(\epsilon\frac{\partial\psi}{\partial x}\right) = -\frac{q}{\epsilon_o}\left[-n + p - N_A^- + N_D^+ + \frac{1}{q}\rho_{def(n,p)}\right] \tag{64}$$

$$-\frac{\partial j_n}{\partial x} + G - U_n(n, p) = \frac{\partial n}{\partial t} \tag{65}$$

$$-\frac{\partial j_p}{\partial x} + G - U_p(n, p) = \frac{\partial p}{\partial t} \tag{66}$$

Where ρ_{pdef} is the defect distribution,U_p, and U_p are the net recombination rates, and G is the generation rate. The generation rate can be calculated using the following equations[73, 74]

$$G(x, \lambda) = \frac{1}{2} c \epsilon \alpha n |E(x)|^2 \tag{67}$$

$$G(x, \lambda) = \frac{\lambda Q(z, \lambda)}{hc} \tag{68}$$

$$G(\lambda) = \int_{1.5G} Q(x, \lambda) d\lambda \tag{69}$$

Where c is the speed of light,α is the absorption coefficient,and Q is the energy dissipation

Chapter 5

5 Results and discussion

5.1 Nanoparticle characterization

The surface morphology and structure of the nickel-cobalt nanoparticles were studied using transmission electron microscopy (TEM) and scanning electron microscopy (SEM) as shown in Figure 17 and Figure 18a. The TEM displays a 2D image of the nanoparticle which shows an irregular circular shape with a size ranging from 29 nm to 74 nm. while the SEM captures a 3D image, which displays various sizes of spherical shape nanoparticles. The white spots in the TEM figures show the nanoparticle is porous.

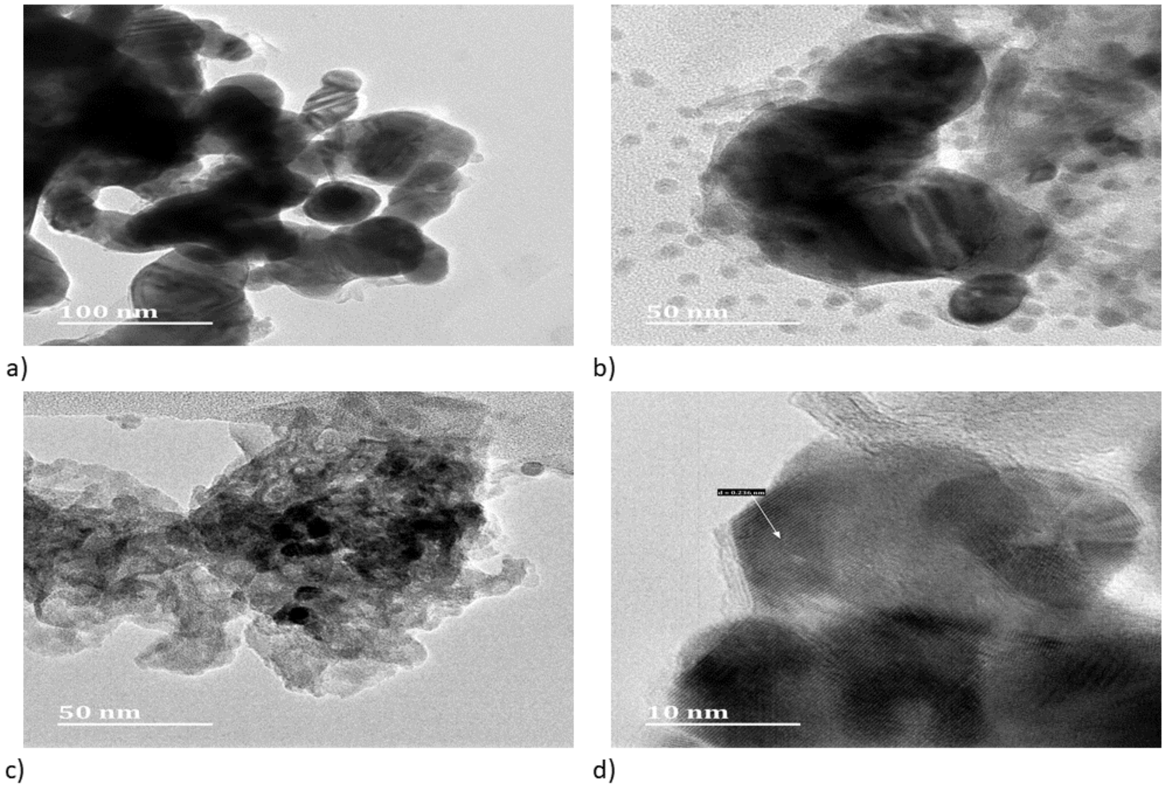

Figure 17: Different resolution of the TEM images of Ni/Co:a) 100 nm, b)50 nm, c) 50 nm and d) 10 nm.

At high resolution(Figure 17d), the fringes are observed with the atomic plane spacing $d = 0.256$ nm. The orientation of the atomic planes is different for each grain or crystalline which therefore confirms the polycrystallinity of the structure as displayed by Figure 17d. The compositions of each nanoparticle(Ni and Co) were studied using the EDS (EDX) analysis(Figure 18). The EDS spectrum depicts the peaks of Ni and Co with no other peaks observed except for these two components, which therefore reveals the purity of the Ni/Co NPs with no defects in the Ni/Co sample, this is further confirmed by Figure 18d which shows that the composition of Co is 35.06 wt % and that of Ni is 64.94 wt % which add up to 100 %.

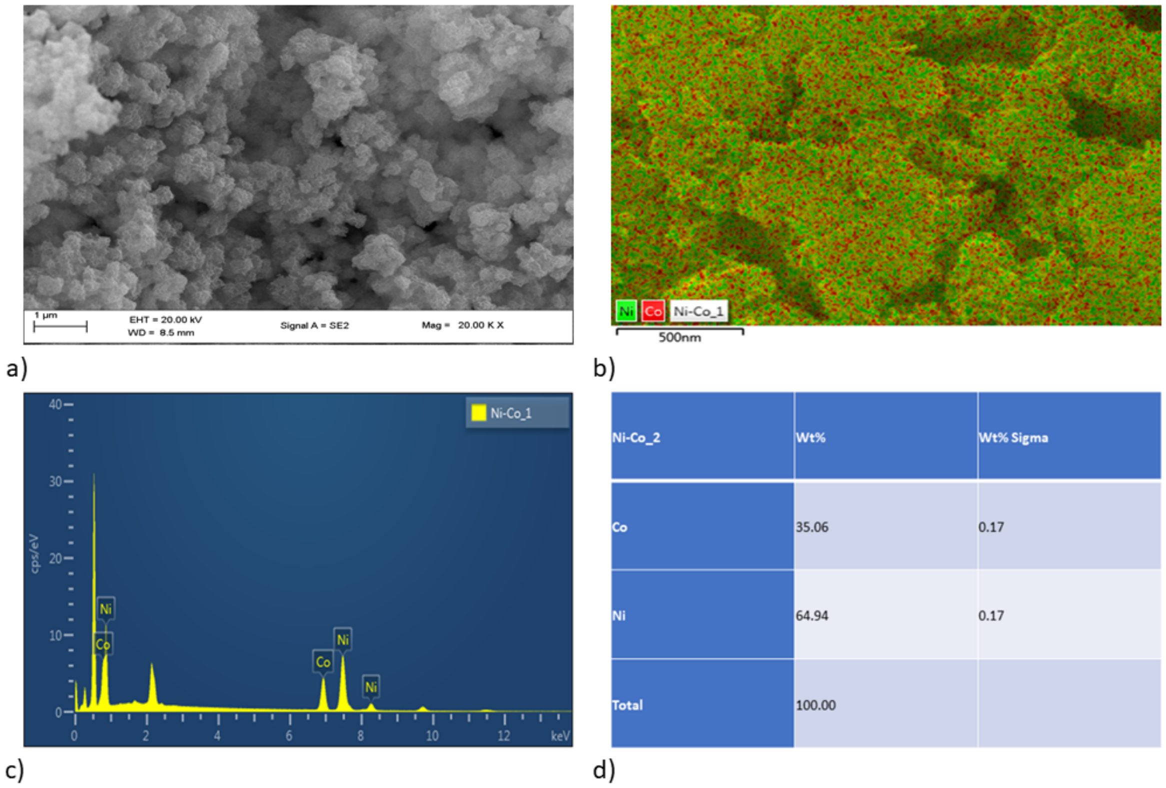

Ni-Co_2	Wt%	Wt% Sigma
Co	35.06	0.17
Ni	64.94	0.17
Total	100.00	

Figure 18: a) & b) SEM images of Ni/Co, c) EDS spectrum of the bi-metallic Np comprises Ni and Co, Ni and cobalt, and the composition of each component.

5.2 Optical absorption of the photovoltaic device with the different NP concentrations

The absorption of light by the device plays very crucial role in solar cells' performance as it influences the photo-current. In this study, we sought to employ a material that can improve the absorption of the solar absorber layers by way of increasing the incident light path length in the device structure. In this search, Ni/Co NPs were incorporated in the hole transport layer of the devices which is aimed at changing the direction of the incident light by reflection and LSPR that promote light trapping in the medium. The impact of the metal nanoparticle is evident on the measured optical absorption spectrum taken from the entire layers of the solar cell structure. The absorbance peak of P3HT:PBCM (Figure 19a black curve) centred at the wavelength of 550 nm is much smaller than the absorbance of the nanoparticle at the same wavelength(Figure 19b). This undoubtedly gave hope that incorporating this NP in the OSC device structure will yield good results. This nanoparticle was then incorporated in the PEDOT:PSS buffer layers, and the optical absorption of the devices were measured. The UV-Vis spectra provided in Figure 19a shows the absorption of the devices with pristine and different concentrations of the Ni/Co BMNPs. The concentration of Ni/Co ranges from 0.05 %(0.5 mg) to 0.25 %(2.5 mg). It can be noted that the devices with Ni/Co BMNPs have an improved absorption than the undoped device, this clearly shows the dependence of the device absorption on the concentration of the Ni/Co BMNPs, and other factors could be plasmonic features of the nanoparticle(explained in section 5.4)

5.3 The J-V characteristic of the photovoltaic device

The performance of the newly fabricated devices can be studied from the measured current versus voltage characteristics. The data was taken both under illumination and dark conditions for different reasons for the investigation. The devices were illuminated with the solar simulator of irradiance 1000 W/cm^2. The J-V results are shown in Figure 20 for the illuminated devices, with the improved maximum power for the doped devices compared to the pristine device. The 0.05 % device yielded the highest results compared to the other devices, with a short circuit current density of 15.31 mA/cm^2 was obtained for this device, Fill-Factor of 58.52 % and the V$_{oc}$ of 0.5632 V, which therefore yielded the efficiency of 5.05 % (see Table 2). This is such a big achievement for a P3HT: PCBM-

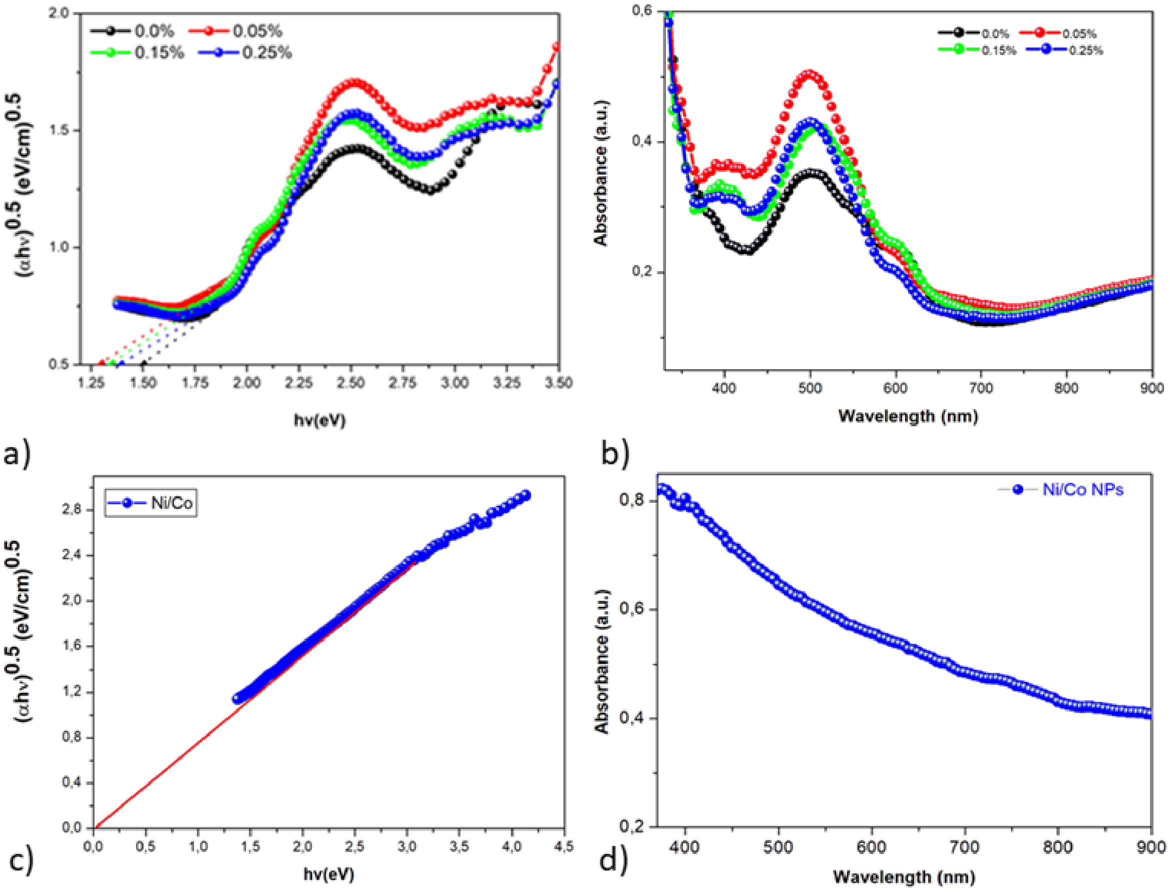

Figure 19: a)Tauc plot used for the calculations of the energy band gap of the devices with doping concentrations ranging from 0 % to 0.25 %. c) Tauc plot used for the calculation of the energy band gap of the Ni/Co Np b) Optical absorption of the P3HT: PCBM device + devices with Ni/Co Nps in the PEDOT:PSS buffer layer. d) optical absorption of Ni/Co Nps.

based device as it can be noted that there is a 67.8 % improvement from the undoped device. As the concentration increases, all the solar cell characteristics parameters are dropping as shown in Table 2 and Figure 20. We therefore summarize the factors that contributed to the improvement and reduction of the device performance, these include the size of the nanoparticle particle which leads to the occurrence of the localized surface plasmon resonance (LSPR), and The interaction of the nanoparticle with the active layer.

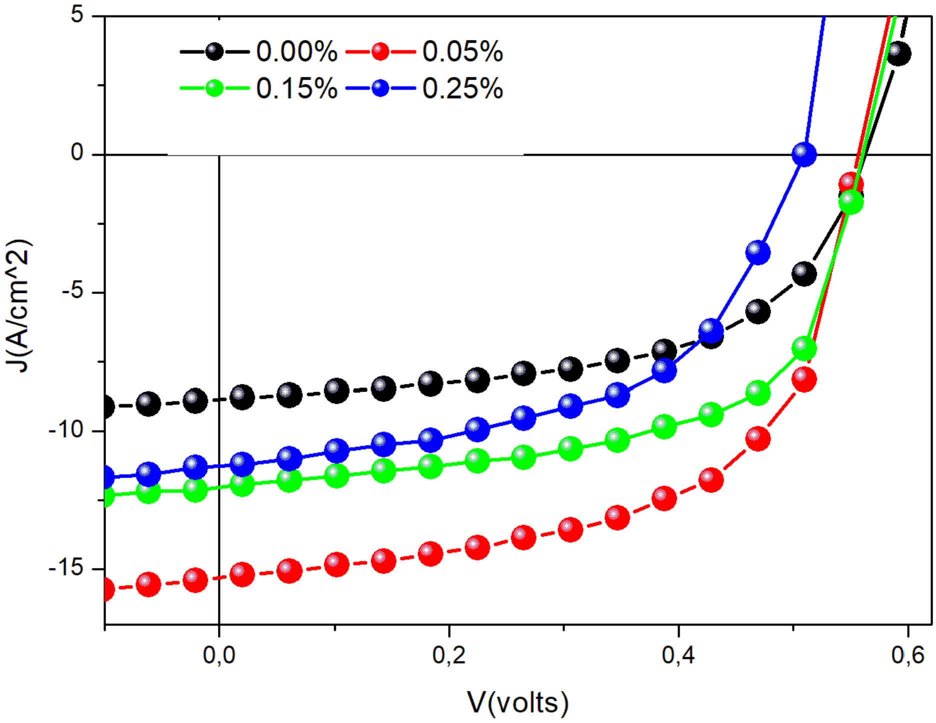

Figure 20: The J-V curves of P3HT:PCBM and Ni/Co Nps at different doping concentrations.

5.4 The effect of the localized surface plasmon resonance

The occurrence of LSPR, which influenced is by the size of the nanoparticle, was what possibly caused the augmentation of the optical absorption of the doped devices. The size of Ni/Co BMNPS is ranging from size from 29 nm to 74 nm based on the measurements taken from the TEM images from Figures 17a and 17b. Eq.56 and eq.57 show the dependence of the absorption and scattering, on the diameter of the nanoparticle, for particles

Table 2: Solar cell characteristic parameters with the concentration of Ni/Co bi-metallic nanoparticle varied from 0.00 % to 0.25 %

Ni/Co wt/ %	V$_{oc}$ /V	J_{sc} /mA/cm^2	FF/%	η/%	R$_s$/Ω	R$_{sh}$/Ω
0.00	0,5704	8.896	54.37	3.01	383	3940
0.05	0.5632	15.31	58.52	5.05	558	11705
0.15	0.5730	11.99	58.75	4.04	628	14225
0.25	0.5062	11.23	55.36	3.15	1098	10340

smaller than or equal to 50 nm [57, 59, 60], absorption dominates the extinction. Consequently, the nanoparticle size influenced the device's absorption of light; this resulted in maximum absorption at 0.05 % concentration, which in turn produced the greatest photo-current and maximum efficiency. As demonstrated by eq.56 and eq.57, scattering predominates over absorption for nanoparticles larger than 50 nm [60]. The scattering is dependent on r^6, and since more light is trapped in the OSCs device, we can infer that the absorption drop as the concentration is increased might have been caused by scattering, which is still greater than Pristine. However, scattering at the HTL layer can positively impact absorptions by increasing the path length of the incident light which increases the chance for light trapping in the medium.

5.5 The interaction of BMNp with the absorber layer

The measured size of the nanoparticle ranges from 20 nm to 74 nm, and the thickness of the buffer layer is maintained at 45 nm. In the case where the diameter of the nanoparticle exceeds the thickness of the buffer layer, the metal and polymer contact(interface) is formed. This contact or interface of the metal to the absorber layer has many effects on the device. The generated electrons from the metal can be transferred to the polymer, and be ready for the generation of the current. This study investigates the influence of this interface on the structure of the polymer. One of the pieces of evidence is the V_{oc}, there is a drastic change in the V_{oc} as the concentration is increased to 0.25 %. It is clear from eq.52 that the V_{oc} depends on the HOMO of the donor material and the LUMO of the acceptor material, so any drastic change in the V_{oc} would have come from the changes in the energy alignments of the absorber material. In the cases of inorganic solar cells, the V_{oc} depends on the bandgap of the absorber material. Observable changes in the band gap would also imply structural changes in the absorber material, Howeverever these changes in the bandgap disagree with the V_{oc} findings (see Table 3), as the theory suggests that the V_{oc} increases with an increasing band gap. So one would have to look at more than just the structural changes to justify the changes in the V_{oc}. We therefore extend our discussion to the recombination of carriers which influences the V$_{oc}$ loss.

5.6 Open circuit voltage loss

The V$_{oc}$ loss in organic solar cells is one of the major factors that impact the power conversion efficiency negatively. The V$_{oc}$ loss ranges from 0.7 eV to 1 eV in OSCs [76] compared to that of inorganic solar cells(such as c-Si, GaAs, CIGS, and perovskite) which are approximately 0.3V[75]. The V$_{oc}$ loss is mainly due to non-radiative recombination, which can be due to high carrier density(auger recombination) [13], holes, and electrons recombining in the electrode(surface recombination, or In the forbidden region (band gap), where doping—which may or may not be intentionally added—forms an energy level, electrons and holes can recombine(Shockley-Read-Hall (SRH or RHS) recombination). Figure 21 summarizes all these recombinations including the radiative recombination.

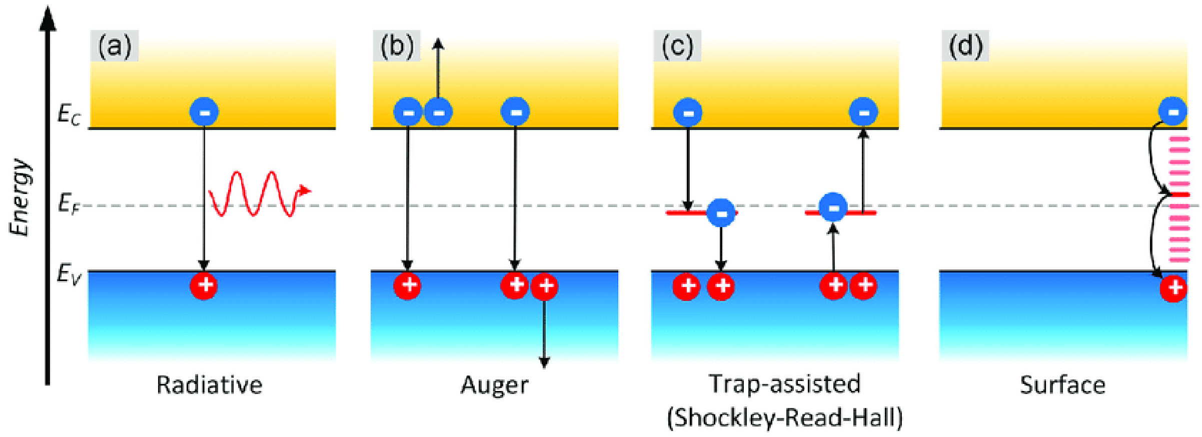

Figure 21: Shows different recombination (radiative and non-radiative), the figure was taken from ref [13].

The V$_{oc}$ loss is defined as

$$q\Delta V = E_g - qV_{oc} \tag{70}$$

Which can also be written as

$$q(\Delta V_1 + \Delta V_2 + \Delta V_3) \tag{71}$$

Where qΔ V$_1$ = (Eg − qV$_{oc}{}^{SQ}$)is the energy difference between bandgap Eg and the Shockley−Queisser limit voltage, qΔ V$_2$ = (qV$_{oc}{}^{SQ}$−qV$_{oc}{}^{rad}$) is voltage loss via radiative recombination from the absorption below bandgap, and Δ V$_3$) = (qV$_{oc}{}^{rad}$ $-$qV$_{oc}$) is voltage loss via nonradiativeEq.70 was used to calculate the $V_{oc}loss$, and the offset energy band gaps for the 4 devices were calculated using the Tauc equation(equation can be found in our previous work ref [17]), which was used to produce Figure 19c, where the optical band gaps are the values in the X-axis pointed by the arrows.The 0.05 % has less V$_{oc}$ loss compared to other devices. This may be due to less recombination as it can be seen in Table 3 that the V$_{oc}$ for 0.05 % device is large. The 0.25 % device has the largest V$_{oc}$ loss, this confirms the occurrence of recombination which affected the V$_{oc}$ and contributed to the drop in efficiency. The type of recombination can not be confirmed due to the lack of tools to calculate them. recombination [75].

Table 3: Charge transport parameters

Ni/Co wt/%	Eg $/eV$	V$_{oc}$ /V	q Δ V /eV	μ_0 x10^{-4} /(cm^2/Vs)	γ/(cm/V)^2
0.00	1.564	0,5704	0.9936	21.60 ± 1.731	-1.0 ±0.2
0.05	1.264	0.5632	0.7008	25.39 ±2.035	-1.7 ±0.2
0.15	1.399	0.5730	0.8260	21.29 ±1.706	-2.4 ±0.2
0.25	1.452	0.5062	0.9458	1.360n±1.090	-1.6 ±0.2

5.7 Dark current

The impact of Ni/Co BMNPs on the charge transport properties in the solar cell is studied by reducing the influence of photons-induced charge generation in the medium. For this reason, the current-voltage characteristics of the devices measured under dark conditions are best for the study of charge transport in the medium. The JV characteristics of devices presented in Figure 22a show the measured data with different doping concentrations of Ni/Co BMNPs in HTL. At the low voltage regions, the JV curves show the Diode JV characteristics [78], with more current being produced by the low concentrations 0.00 % and the 0.05 % doped devices than the other devices(see Figure 22a). This indicates the dominance of holes in the organic solar cells, and the Ni/Co BMNPs have less contribution in terms of improving the dark current since its influence relies on the presence of light.

The current is reduced by increasing the nanoparticle's concentration. At high voltage, all the traps are filled [78], and the current reaches saturation(See Figure 22b), this can be used to extract mobilities by using the space charge limited current model.

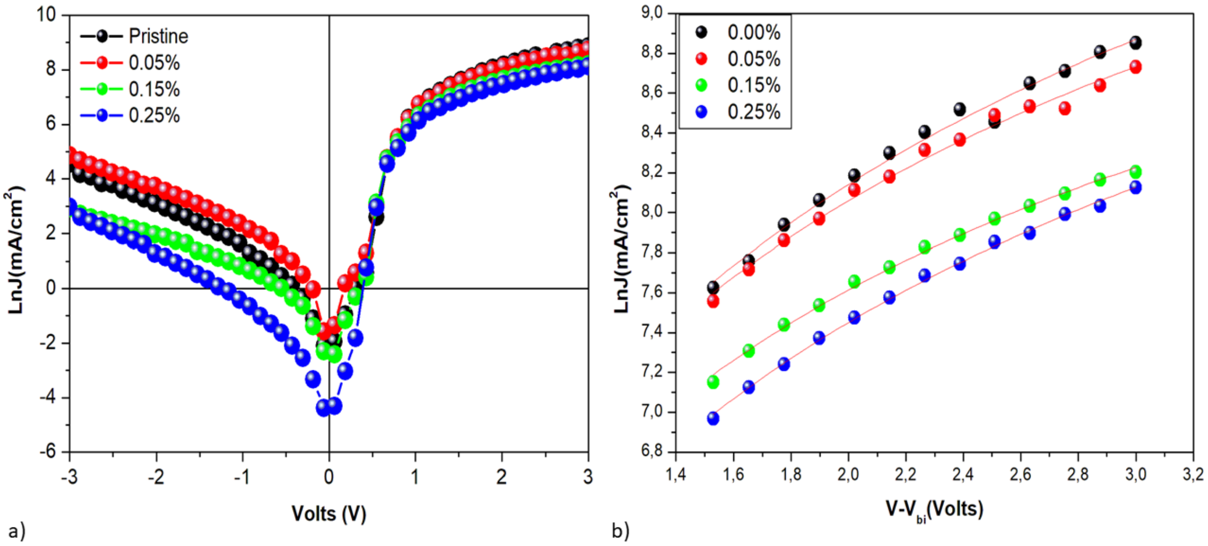

Figure 22: a) Dark JV curves of devices with different doping concentrations,b) Field-dependent space charge limited current plotted with varying doping concentrations.

5.8 Charge carrier mobility

For dark injection, ITO/PEDO: PSS anodes were used to assist hole injection. The PEDOT: PSS and P3HT are expected to form an ohmic contact Since their HOMO levels are equal(HOMO-level = 5.2 eV). Normally an ohmic contact is formed when the conduction bands of the two materials are equal, which is important in determining the electron mobility, however, organic solar cells are made of materials that are rich in holes, hence hole mobilities are calculated using the space charge limited current by the Mott Guenney law given in eq.38. The hole mobility can be calculated when the current reaches saturation(as shown in Figure 22b) such that the resultant voltage drop across the active layer would be defined as[77];

$$V = V_{ap} - V_{bi} \tag{72}$$

where V_{ap} is the applied bias voltage, and V_{bi} is the built-in potential. The field-dependent mobility μ, typical of the Poole-Frenkel-like, can be described by an equation of the form;

$$\mu = \mu_0 \exp\left(\gamma\sqrt{E}\right) \tag{73}$$

Eq.38 can be modified by substituting eq.73 into it

$$J = \frac{9}{8}\varepsilon\varepsilon_0\mu_0 \exp\left(0.89\gamma\sqrt{\frac{V}{L}}\right)\frac{V^2}{L^3} \tag{74}$$

where μ_0 is the low-field mobility and γ field activation factor.The current density and voltage data were fitted with the natural logs of eq.74, for the calculations of the hole mobilities with the concentration of the nanoparticle being varied from 0.05 % – 0.25%. The results are shown in Table 3 for hole mobilities, with fewer changes observed in all the devices, however, the little changes observed show that the devices with 0.05 % have improved mobilities, which can be due to reduced series resistance compared to 0.15 % and 0.25 % devices as shown in Table 2. It can be observed that as the concentration of the nanoparticle is increased the hole mobilities are decreasing. Taking certain metallic properties like mobilities into account, this may be justified. Unlike semiconductors, metals do not have hole mobilities because moving electrons do not leave holes behind. Thus, we might propose that the reason for the decreased hole mobilities as the bi-metal nanoparticle concentration rises is that the nanoparticle blocks holes and prevents them from conducting.

5.9 Simulation results

A device simulation program known as SCAPS was used to reproduce the experimentally observed solar cell performances by computational methods. This effort will provide evidences not only on the device parameters but also on the understanding of the impact of BMNPs employed in the PEDOT:PSS buffer layer however, It should be noted, though, that SCAPS is not capable of supporting numerical computations for metals neither organic solar cells. Furthermore, because it was designed to mimic inorganic (semiconductors) solar cells, it does not support the plasmonic properties of nanoparticles. Nevertheless, numerical computations of this device may be carried out in SCAPS if the physical parameters of the blended P3HT:PCBM(or any other organic materials) are known. To investigate the effect of Ni/Co BMNPs on the P3HT: PCBM-based device's performance, The method used in ref [81] was to add the Ni/Co BMNPs to SCAPS as a core buffer layer. Nevertheless, this was not feasible since there were no physical parameters(such as hole mobilities) that would have made the Ni/Co BMNPs fit inside SCAPS. After that, The experimental results were examined to determine which parameters were impacted by the Ni/Co BMNPs' presence. One of them, the energy band gap, showed noticeable variations. In this investigation, an effort was made to adjust the band gap using the exact experimental values (taken from Table 2), but the results were exaggerated(not shown here), and the EQE widened more than was reasonable for any P3HT: PCBM-based device, particularly for energy band gap values below 1.5 eV. It is then modified to 1.8 eV for the pristine device, which was previously employed in our work in ref [81]. Additionally, the band gap values were adjusted to 1.7 eV, 1.6 eV, and 1.5 eV, respectively, to mimic the 0.25 %, 0.15 %, and 0.05 % doped devices.

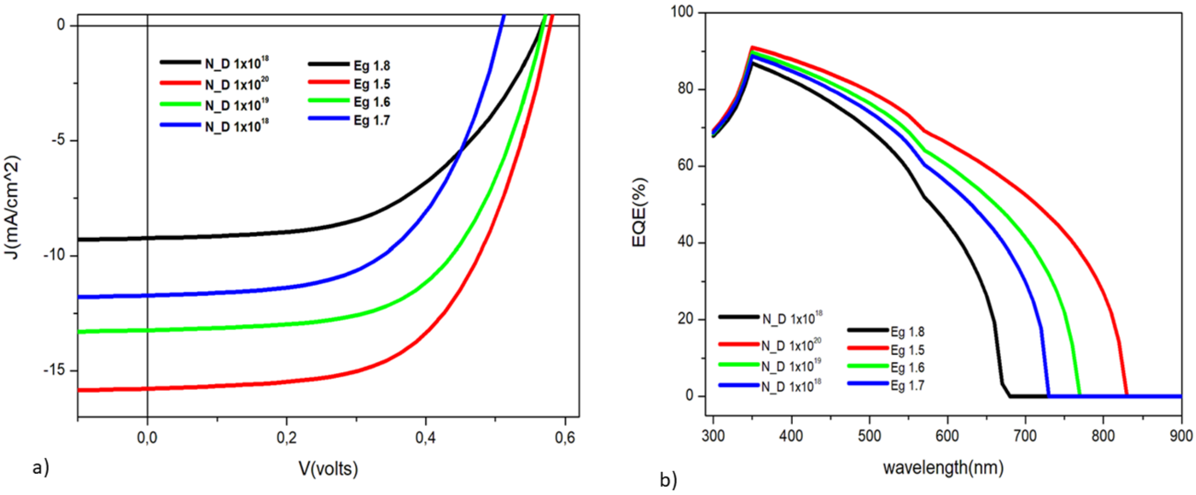

Figure 23: a) JV curves and b) EQE plotted against different values of absorber layer energy band gap, and Hole transport layer density of donors.

It's more than just an energy band gap examined to investigate the effect of the

Ni/Co BMNPs, however, all the parameters needed in the simulation program could not be located since we did not have the necessary equipment in our lab. As a result, some of the techniques used in ref [79, 80] were adopted, which deal with acceptor and donor densities. For this reason, parameters were changed to PEDOT:PSS buffer layer's acceptor and donor densities. Varying the density of acceptors showed no changes at all (not reported here), however, Varying the density of donors of the PEDOT:PSS buffer layer caused significant changes in the device performance. The band gap values and the density of donors were simultaneously varied as shown in Table 4. The results show observable similarities between the experimental and simulated results, especially the JV curves display the same trend (see Figure 20 and Figure 23a). The 1x10^{18}, Eg 1.8 eV which was made to mimic the 0.00 % experimental device has produced an efficiency of 3.07 % which is very close to the experimental result of 3.01 % of 0.00 % device. The 0.05 % device was mimicked by the N_D 1x10^{20}, Eg 1.5 eV device, the simulated device shows much improvement efficiency of 5.76 %, however other parameters such as V_{oc}, J_{sc}, and FF are very close to that obtained experimentally. It was necessary to decrease the donor densities while raising the energy band gap values, to computationally produce results that are equivalent to those of 0.15 % and 0.25 % devices (see Table 4 and Figure 23a. External quantum efficiency calculations were carried out, as indicated in Figure 23b, to find out how much of the incoming photons were collected. The highest EQE is observed in the N_D 1x10^{20}, Eg 1.8 eV device. The graph generated with Eg =1.8 eV device is narrow compared to the other devices. When the energy band gap is big, only the energetic photons can be absorbed, however when the energy band gap is small both the

Table 4: Solar cell characteristic parameters with different values of absorber layer energy band gap, and Hole transport layer density of donors.

Ni/Co wt/ %	N_D/cm^{-3}	Eg/eV	V_{oc} /V	J_{sc} /mA/cm^2	FF/ %	η/%
0.00	1x 10^{18}	1.8	0.5668	9.244	52.68	3.07
0.05	1x 10^{20}	1.5	0.5768	15.76	57.76	5.76
0.15	1x 10^{19}	1.6	0.5684	13.22	58.22	4.86
0.25	1x 10^{18}	1.7	0.5159	11.71	55.77	3.74

energetic photons and the less energetic photons are absorbed [81] hence the EQE shifts to the red region for small band gap devices. The results of the computational simulations were constrained by the fact that the SCAPS program does not support LSPR properties of materials, in contrast to the experimental work which demonstrates that the improved optical absorption was caused by the occurrence of LSPR and no red shift was observed even for small band gap devices(see figure 19b).

Chapter 6

6 Conclusions

The Ni/Co BMNPS were successfully synthesized using the chemical reduction method. The morphology and size of the Ni/Co bi-metallic NPs were studied using high-resolution TERM and SEM. The evidence suggests that there are indications of spherical shape of the Ni/Co Nps with the size ranging from 29 nm to 74 nm. Using EDX analysis, the composition of each component (Ni and Co) was examined; the results confirmed no defects in the sample were detected. The Ni/Co was incorporated in the PEDOT:PSS buffer layer with different doping concentrations ranging from 0.0 % to 0.25 %. A device architecture with layers of materials such as ITO/PEDOT:PSS(Ni/Co %)/P3HT:PCBM/LiF/Al, was used for all types of solar cells produced in this investigation. Measurements of the optical absorption demonstrated the concentration dependency of the optical absorption, with a significant improvement for doped devices. The voltage-current density measurements, which generate the device parameters, suggest that enhanced photon absorption due to the occurrence of LSPR led to a significant improvement in power conversion efficiency as high as 67 % at 0.05 % doping level compared to the pristine device. As the concentration increases there is a reduction attributed to the V_{oc} loss brought on by carrier recombination, the main factor for the sharp decline in the V_{oc} for the 0.25 % device. Furthermore, a series of device simulations were conducted using the SCAPS program, to reproduce the experimental results. The energy band gap of the absorber layer was varied simultaneously with the density of donors of the PEDOT:PSS buffer layer to take into account the effect of Ni/Co. The highest efficiency of 5.74 % was obtained from the Eg = 1.5 eV, N_D $1x10^{20}$ device with 88 % improvement in PCE from the pristine device. Moreover, the devices with the lowest band gaps showed wider EQE graphs than the high energy band gap devices, which displayed a narrow EQE graph due to the inability to absorb high energetic photons. overall doped devices showed better performance than the undoped devices for both experiments and simulation. In summary, the use of this nanoparticle in the hole transport layer can effectively improve device performance in OSC and based on non-fullerene acceptors.

References

[1] Wolfgang, T., 2011. *Device Physics of Organic Solar Cells* . Dresden .Technische Universitat Dresden, pp. 1- 364.

[2] Kalogirou, S.A., 2009. *Solar energy engineering: processes and systems.* Academic press, pp. 1- 779

[3] Sesa, E., 2013. *A novel electrical model for organic photovoltaic cells.* Newcastle. University of Newcastle, pp. 1- 201.

[4] Jamshidi, M., Hatch, A., Lowery, A.D. and Smith, J.E., 2017. *The Future of Solar Energy.* International Journal of Contemporary ENERGY, 3(2), pp.8-15.

[5] Moriarty, P. and Honnery, D., 2012. *What is the global potential for renewable energy?.* Renewable and Sustainable Energy Reviews, 16(1), pp.244-252.

[6] Kaltschmitt, M., Streicher, W. and Wiese, A. eds., 2007. *Renewable energy: technology, economics and environment.* Springer Science & Business Media, pp. 1- 564.

[7] Shahzad, U., 2012. *The need for renewable energy sources.* energy, 2, pp.16-18.

[8] Brusso, B.C., 2019. *A brief history of the energy conversion of light [history].* IEEE Industry Applications Magazine, 25(4), pp.8-13.

[9] Rohr, J., 2018. *Measurements and modelling of space-charge-limited current transport in organic single-carrier devices.* London. Imperial College London, pp. 1- 248.

[10] Doumon, N.Y., 2019. *The degradation of organic solar cells: From chemistry to device physics through materials.* University of Groningen, [Groningen] https://doi.org/10.33612/diss.98539626

[11] NREL (2023) Best Research-Cell Eficiency Chart. Available at: https://www.nrel.gov/pv/cell-efficiency.html (Accessed: 11 January 2024)

[12] Köhler, A. and Bässler, H., 2015. *Electronic processes in organic semiconductors: An introduction.* John Wiley and Sons,pp. 1- 405.

[13] Plakhotnyuk, M., 2018. *Nanostructured Heterojunction Crystalline Silicon Solar Cells with Transition Metal Oxide Carrier Selective Contacts.* DTU Nanotech, PP. 1-182.

[14] Yao, H. and Hou, J., 2022. *Recent Advances in Single-Junction Organic Solar Cells.* Angewandte Chemie, 134(37), p.e202209021.

[15] Luo, D., Jang, W., Babu, D.D., Kim, M.S., Wang, D.H. and Kyaw, A.K.K., 2022. *Recent progress in organic solar cells based on non-fullerene acceptors: materials to devices.* Journal of Materials Chemistry A, 10(7), pp.3255-3295.

[16] Zhu, L., Zhang, M., Zhong, W., Leng, S., Zhou, G., Zou, Y., Su, X., Ding, H., Gu, P., Liu, F. and Zhang, Y., 2021. *Progress and prospects of the morphology of non-fullerene acceptor based high-efficiency organic solar cells.* Energy & Environmental Science, 14(8), pp.4341-4357.

[17] Ike, J.N., Jili, N., Kumar, A., Sharma, G. and Mola, G.T., 2023. *The impact of Ag/Co nanocomposite on organic charge transport medium for improved photocurrent in polymer solar cell.* Journal of Polymer Science, 61(21), pp.2721-2732.

[18] Hamed, M.S., Ahmed, A.Y. and Mola, G.T., 2023. *Suppressing charge recombination in disordered polymers blend medium.* Journal of Physics D: Applied Physics, 56(40), p.405101.

[19] Gebremariam, K.G., Hone, F.G., Dai, J., Mola, G.T., Mammo, W. and Tegegne, N.A., 2023. *Effect of an ambient environment on light-induced degradation of organic solar cells based on a benzodithiophene–quinoxaline copolymer in air.* New Journal of Chemistry, 47(28), pp.13331-13341.

[20] Böer, K.W. and Pohl, U.W., 2023. *Properties and Growth of Semiconductors.* In Semiconductor Physics. Cham: Springer International Publishing,pp. 3-34

[21] Sze, S.M., Li, Y. and Ng, K.K., 2021. *Physics of semiconductor devices.* John wiley & sons, pp. 1-931.

[22] Kittel, C., 2005. *Introduction to solid state physics.* John Wiley & sons, pp. 1-680.

[23] Neamen, D.A., 2012. *Semiconductor physics and devices: basic principles.*McGraw-Hill, pp. 1- 758.

[24] Zekry, A., Shaker, A. and Salem, M., 2018. *Solar cells and arrays: principles, analysis, and design.* In Advances in renewable energies and power technologies.Elsevier, pp. 3-56.

[25] Zeman, M., 2003. *Introduction to photovoltaic solar energy.* Delft University of Technology, 2(6), pp. 1.1- 8.16.

[26] Goetzberger, A. and Hoffmann, V.U., 2005. *Photovoltaic solar energy generation* . Springer Science & Business Media.(Vol. 112), pp. 1- 234.

[27] Fahrenbruch, A. and Bube, R., 1983. *Fundamentals of solar cells: photovoltaic solar energy conversion.*California. Elsevier, pp. 1- 558.

[28] Reinders, A., Verlinden, P., Van Sark, W. and Freundlich, A., 2017. *Photovoltaic solar energy: from fundamentals to applications.* John Wiley & Sons, pp. 1- 181.

[29] Murgatroyd, P.N., 1970. *Theory of space-charge-limited current enhanced by Frenkel effect.* Journal of Physics D: Applied Physics, 3(2), p.151.

[30] Röhr, J.A., Moia, D., Haque, S.A., Kirchartz, T. and Nelson, J., 2018. *Exploring the validity and limitations of the Mott–Gurney law for charge-carrier mobility determination of semiconducting thin-films.* Journal of Physics: Condensed Matter, 30(10), p.105901.

[31] Myers, R.J., 2008. 5.5. 2 *Applying The Universal Mobility Law To The Mott-Gurney Law.* LIVERPOOL, p.149.

[32] Sun, J.X., Yang, H.C., Li, Y. and Cui, H.J., 2023. *Analytic Solutions of Drift-Diffusion Equations and Mobility of Organic Semiconductors.* Physical Review Applied, 20(3), p.034061.

[33] Mdluli, S.B., Ramoroka, M.E., Yussuf, S.T., Modibane, K.D., John-Denk, V.S. and Iwuoha, E.I., 2022. *π-Conjugated polymers and their application in organic and hybrid organic-silicon solar cells.* Polymers, 14(4), p.716.

[34] Servaites, J.D., Ratner, M.A. and Marks, T.J., 2011. *Organic solar cells: A new look at traditional models.* Energy & Environmental Science, 4(11), pp.4410-4422.

[35] Yeh, N. and Yeh, P., 2013. *Organic solar cells: Their developments and potentials.* Renewable and Sustainable Energy Reviews, 21, pp.421-431.

[36] Abdulrazzaq, O.A., Saini, V., Bourdo, S., Dervishi, E. and Biris, A.S., 2013. Organic solar cells: a review of materials, limitations, and possibilities for improvement. Particulate science and technology, 31(5), pp.427-442.

[37] Bagher, A.M., 2014. *Introduction to organic solar cells.* Sustainable Energy, 2(3), pp.85-90.

[38] Kumar, P. and Chand, S., 2012. *Recent progress and future aspects of organic solar cells. Progress in Photovoltaics*: Research and applications, 20(4), pp.377-415.

[39] Zhao, F., Wang, C. and Zhan, X., 2018. *Morphology control in organic solar cells.* Advanced Energy Materials, 8(28), p.1703147.

[40] Dimitrov, S.D. and Durrant, J.R., 2014. *Materials design considerations for charge generation in organic solar cells.* Chemistry of Materials, 26(1), pp.616-630.

[41] Steim, R., Kogler, F.R. and Brabec, C.J., 2010. Interface materials for organic solar cells. Journal of Materials Chemistry, 20(13), pp.2499-2512.

[42] Qi, B. and Wang, J., 2012. *Open-circuit voltage in organic solar cells.* Journal of Materials Chemistry, 22(46), pp.24315-24325.

[43] Yang, F. and Forrest, S.R., 2008. *Photocurrent generation in nanostructured organic solar cells.* ACS nano, 2(5), pp.1022-1032.

[44] Zhang, F., Xu, X., Tang, W., Zhang, J., Zhuo, Z., Wang, J., Wang, J., Xu, Z. and Wang, Y., 2011. *Recent development of the inverted configuration organic solar cells.* Solar Energy Materials and Solar Cells, 95(7), pp.1785-1799.

[45] Schlenker, C.W. and Thompson, M.E., 2011. *The molecular nature of photovoltage losses in organic solar cells.* Chemical communications, 47(13), pp.3702-3716.

[46] Clarke, T.M. and Durrant, J.R., 2010. *Charge photogeneration in organic solar cells.* Chemical reviews, 110(11), pp.6736-6767.

[47] Peumans, P., Yakimov, A. and Forrest, S.R., 2003. *Small molecular weight organic thin-film photodetectors and solar cells.* Journal of Applied Physics, 93(7), pp.3693-3723.

[48] Woo, S., Jeong, J.H., Lyu, H.K., Han, Y.S. and Kim, Y., 2012. *In situ-prepared composite materials of PEDOT: PSS buffer layer-metal nanoparticles and their application to organic solar cells.* Nanoscale Research Letters, 7, pp.1-6.

[49] Mirsakiyeva, A., 2017.*Electronic and optical properties of conducting polymers from quantum mechanical computations.*Stockholm.Diva-portal, pp. 1- 54.

[50] Li, Y., Huang, W., Zhao, D., Wang, L., Jiao, Z., Huang, Q., Wang, P., Sun, M. and Yuan, G., 2022. *Recent progress in organic solar cells: a review on materials from acceptor to donor.* Molecules, 27(6), p.1800.

[51] Luscombe, C.K., Maitra, U., Walter, M. and Wiedmer, S.K., 2021. *Theoretical background on semiconducting polymers and their applications to OSCs and OLEDs.* Chemistry Teacher International, 3(2), pp.169-183.

[52] Heeger, A.J., 2001. *Nobel Lecture: Semiconducting and metallic polymers: The fourth generation of polymeric materials.* Reviews of Modern Physics, 73(3), p.681.

[53] Anabestani, H., Nabavi, S. and Bhadra, S., 2022. *Advances in Flexible Organic Photodetectors: Materials and Applications*. Nanomaterials, 12(21), p.3775.

[54] Hoppe, H. and Sariciftci, N.S., 2004. *Organic solar cells: An overview*. Journal of materials research, 19(7), pp.1924-1945.

[55] Cai, W., Gong, X. and Cao, Y., 2010. *Polymer solar cells: recent development and possible routes for improvement in the performance*. Solar energy materials and solar cells, 94(2), pp.114-127.

[56] Abrahamsson, T., 2021. *Synthetic Functionalities for Ion and Electron Conductive Polymers: Applications in Organic Electronics and Biological Interfaces* (Doctoral dissertation, Linköping University Electronic Press).

[57] Ghobadi, T.G.U., Ghobadi, A., Ozbay, E. and Karadas, F., 2018. *Strategies for plasmonic hot-electron-driven photoelectrochemical water splitting*. ChemPhotoChem, 2(3), pp.161-182.

[58] Ye, Z., Xu, Z., Yue, W., Liu, X., Wang, L. and Zhang, J., 2023. *Exploiting the LSPR effect for an enhanced photocatalytic hydrogen evolution reaction*. Physical Chemistry Chemical Physics, 25(4), pp.2706-2716.

[59] Li, Y.F., Kou, Z.L., Feng, J. and Sun, H.B., 2020. *Plasmon-enhanced organic and perovskite solar cells with metal nanoparticles*. Nanophotonics, 9(10), pp.3111-3133.

[60] Uddin, A. and Yang, X., 2014. *Surface plasmonic effects on organic solar cells*. Journal of nanoscience and nanotechnology, 14(2), pp.1099-1119.

[61] Rycenga, M., Cobley, C.M., Zeng, J., Li, W., Moran, C.H., Zhang, Q., Qin, D. and Xia, Y., 2011. *Controlling the synthesis and assembly of silver nanostructures for plasmonic applications*. Chemical reviews, 111(6), pp.3669-3712.

[62] Wang, L., Hasanzadeh Kafshgari, M. and Meunier, M., 2020. *Optical properties and applications of plasmonic-metal nanoparticles*. Advanced Functional Materials, 30(51), p.2005400.

[63] Stratakis, E. and Kymakis, E., 2013. *Nanoparticle-based plasmonic organic photovoltaic devices.* Materials Today, 16(4), pp.133-146.

[64] Anderson, L.J., Mayer, K.M., Fraleigh, R.D., Yang, Y., Lee, S. and Hafner, J.H., 2010. Quantitative measurements of individual gold nanoparticle scattering cross sections. The Journal of Physical Chemistry C, 114(25), pp.11127-11132.

[65] Notarianni, M., Vernon, K., Chou, A., Aljada, M., Liu, J. and Motta, N., 2014. *Plasmonic effect of gold nanoparticles in organic solar cells.* Solar Energy, 106, pp.23-37.

[66] Kalfagiannis, N., Karagiannidis, P.G., Pitsalidis, C., Panagiotopoulos, N.T., Gravalidis, C., Kassavetis, S., Patsalas, P. and Logothetidis, S., 2012. *Plasmonic silver nanoparticles for improved organic solar cells.* Solar Energy Materials and Solar Cells, 104, pp.165-174.

[67] Mola, G.T., Mthethwa, M.C., Hamed, M.S., Adedeji, M.A., Mbuyise, X.G., Kumar, A., Sharma, G. and Zang, Y., 2020. *Local surface plasmon resonance assisted energy harvesting in thin film organic solar cells.* Journal of Alloys and Compounds, 856, p.158172.

[68] Petryayeva, E. and Krull, U.J., 2011. *Localized surface plasmon resonance: Nanostructures, bioassays and biosensing—A review.* Analytica chimica acta, 706(1), pp.8-24.

[69] Burgelman, M., Decock, K., Niemegeers, A., Verschraegen, J. and Degrave, S., 2016. *SCAPS manual.* University of Ghent: Ghent, Belgium, pp. 1- 146.

[70] Lin, K.T., Lin, H. and Jia, B., 2020. *Plasmonic nanostructures in photodetection, energy conversion and beyond.* Nanophotonics, 9(10), pp.3135-3163.

[71] Boriskina, S.V., Ghasemi, H. and Chen, G., 2013. *Plasmonic materials for energy: From physics to applications.* Materials Today, 16(10), pp.375-386.

[72] Minbashi, M., Ghobadi, A., Ehsani, M.H., Dizaji, H.R. and Memarian, N., 2018. *Simulation of high efficiency SnS-based solar cells with SCAPS.* solar energy, 176, pp.520-525.

[73] Zidan, M.N., Ismail, T. and Fahim, I.S., 2021. *Effect of thickness and temperature on flexible organic P3HT: PCBM solar cell performance.* Materials Research Express, 8(9), p.095508.

[74] Sreedhar Ram, K., Mehdizadeh-Rad, H., Ompong, D., Setsoafia, D.D.Y. and Singh, J., 2021. *Characterising Exciton Generation in Bulk-Heterojunction Organic Solar Cells.* Nanomaterials, 11(1), p.209.

[75] Liu, J., Xian, K., Ye, L. and Zhou, Z., 2021. *Open-Circuit Voltage Loss in Lead Chalcogenide Quantum Dot Solar Cells.* Advanced Materials, 33(29), p.2008115.

[76] Menke, S.M., Ran, N.A., Bazan, G.C. and Friend, R.H., 2018. *Understanding energy loss in organic solar cells: toward a new efficiency regime.* Joule, 2(1), pp.25-35.

[77] Tessema, G., 2012. *Charge transport across bulk heterojunction organic thin film.* Applied Physics A, 106, pp.53-57.

[78] Ogundele, A.K. and Mola, G.T., 2022. *Ternary atoms alloy quantum dot assisted hole transport in thin film polymer solar cells.* Journal of Physics and Chemistry of Solids, 171, p.110999.

[79] Al-Mudhaffer, M.F. and Al-Asadi, A.S., 2021. *Optimization of nanoparticle organic photovoltaic device performance using SCAPS software.* Journal of Electronic Materials, 50(8), pp.4663-4670.

[80] Adedeji, M.A. and Mola, G.T., 2022. *Numerical investigation of the effects of copper sulfide nanoparticles on hole transport layer of thin-film organic solar cells.* Journal of Computational Electronics, 21(1), pp.128-136.

[81] Jili, N., Dlamini, N. and Mola, G.T., 2023. *Computational investigation of the effect ZnS buffer layer on the hole transport of polymer solar cell*. Physica B: Condensed Matter, 666, p.415122.